Divertor Tokamak Test facility project: status of design and implementation

Mastrostefano, S.; Mattei, M.; Mauro, G.; Mauro, S.; Meineri, C.; Melaragni, L.; Mele, A.; Meller, P.; Meloni, S.; Menicucci, I.; Messina, G.; Mezi, L.; Miccichè, G.; Micheletti, M.; Migliori, S.; Milanesio, D.; Milazzo, F.; Milazzo, R.; Minelli, P.; Minucci, S.; Mirizzi, F.; Missirlian, M.; Monarca, D.; Monti, C.; Mori, M.; Moriani, A.; Morici, L.; Moro, A.; Moro, A.; Moro, F.; Mosetti, P.; Mozzillo, R.; Murari, A.; Muraro, A.; Murra, D.; Muscente, P.; Musumeci, S.; Muzzi, L.; Nallo, G. F.; Napoli, F.; Nardon, E.; Naselli, E.; Neu, R.; Nocente, M.; Notazio, M.; Nowak, S.; Ocello, E.; Oliva, A.; Orsetti, V.; Orsini, A.; Orsitto, F. P.; Ortino, M.; Ottavi, M.; Paccagnella, G.; Pacella, D.; Pagani, I.; Paganucci, N.; Pagliaro, A.; Palazzolo, V.; Palermo, M.; Palomba, S.; Panza, F.; Paoletti, D.; Parisi, M.; Pasqualotto, R.; Passarello, S.; Passoni, M.; Patton, T.; Pelliccia, L.; Peloso, A.; Pepato, A.; Perelli, E.; Perencin, A.; Peruzzo, S.; Pesenti, A.; Pedroni, N.; Petrolini, P.; Piergotti, V.; Pidatella, A.; Pigatto, L.; Pillon, M.; Pinna, T.; Pipolo, S.; Piras, S.; Piron, C.; Piron, L.; Pironti, A.; Pistilli, M.; Placido, D.; Pizzuto, A.; Platania, P.; Polimadei, A.; Pollastrone, F.; Polli, G. M.; Pomaro, N.; Pompili, F.; Ponti, C.; Porcelli, F.; Prandelli, V.; Previti, A.; Princiotta, A.; Pucino, G.; Quaglia, F.; Quercia, A.; Raffaelli, F.; Ramogida, G.; Ranieri, G.; Raspante, B.; Ravarotto, D.; Ravera, G. L.; Reale, A.; Rebesan, P.; Recchia, M.; Regine, D.; Renno, F.; Riccardi, B.; Ricci, D.; Rigamonti, D.; Ripani, M.; Rispoli, N.; Roccella, S.; Rocchi, G.; Roche, H.; Romanato, M.; Romanelli, F.; Romanelli, F.; Romanelli, G.; Romaniello, R.; Romano, A.; Romano, M.; Romano, R.; Rossi, R.; Rubinacci, G.; Rubino, G.; Rubino, G.; Rubino, S.; Rueda Rueda, J.; Rufoloni, A.; Salvia, C.; Salvini, P.; Scarpari, M.; Salvitti, A.; Salvò, L.; Sandri, S.; Santoro, F.; Satriano, A.; Savoldi, L.; Scardino, C.; Schettini, G.; Schmuck, S.; Scionti, J.; Scisciò, M.; Scungio, M.; Sedlak, K.; Senni, L.; Sias, G.; Sibio, A.; Simonetto, A.; Singh, L.; Sirignano, A.; Sozzi, C.; Spada, I.; Spagnolo, S.; Spinicci, L.; Spizzo, G.; Spolaore, M.; Stefanini, C.; Strobel, H.; Subba, F.; Taccogna, F.; Taheri, B.; Tantos, C.; Tarallo, A.; Tarantino, M.; Tardini, G.; Tardocchi, M.; Tarfila, P.; Tenaglia, A.; Terlizzi, C.; Terranova, D.; Testa, D.; Testa, E.; Testoni, R.; Toigo, V.; Torrisi, G.; Trotta, A.; Trovato, G.; Tsitrone, E.; Tuccillo, A.; Tudisco, O.; Turcato, M.; Turtù, S.; Uccello, A.; Ugoletti, M.; Uras, O.; Uras, M.; Utili, M.; Vaccaro, V.; Valentini, F.; Valletti, L.; Valisa, M.; Van Eester, D.; Vanzan, D.; Vassallo, E.; Vecchi, G.; Vellucci, M.; Venneri, I.; Ventura, G.; Veranda, M.; Verdini, L.; Verona, C.; Verona Rinati, G.; Veronese, F.; Vianello, N.; Viganò, F.; Villano, O.; Villari, R.; Villone, F.; Vincenzi, P.; Vitale, V.; Vivio, F.; Vlad, G.; Wischmeier, M.; Wu, H. S.; Wyss, I.; Zanino, R.; Zaniol, B.; Zanon, F.; Zappatore, A.; Zavarise, G.; Zito, P.; Zoppoli, A.; Zucchetti, M.; Zuin, M.; Zumbolo, P.. - In: NUCLEAR FUSION. - ISSN 0029-5515. - ELETTRONICO. - 64:11(2024). [10.1088/1741-4326/ad5740]

PAPER • OPEN ACCESS

Divertor Tokamak Test facility project: status of design and implementation

To cite this article: Francesco Romanelli *et al* 2024 *Nucl. Fusion* **64** 112015

OPEN ACCESS
IOP Publishing | International Atomic Energy Agency
Nuclear Fusion
Nucl. Fusion **64** (2024) 112015 (23pp)
https://doi.org/10.1088/1741-4326/ad5740

Divertor Tokamak Test facility project: status of design and implementation

Francesco Romanelli[1,48,*] on behalf of DTT Contributors: D. Abate[43], E. Acampora[10], D. Agguiaro[30], R. Agnello[43], P. Agostinetti[43,54], M. Agostini[43], A. Aimetta[41], R. Albanese[1,10], G. Alberti[40], M. Albino[39], E. Alessi[6], S. Almaviva[11], M. Alonzo[11], R. Ambrosino[1,10], P. Andreoli[11], M. Angelone[48], M. Angelucci[11], C. Angioni[34], A. Angrisani Armenio[11], P. Antonini[22], D. Aprile[43], G. Apruzzese[11], M. Aquilini[11], G. Aragone[2], P. Arena[12], M. Ariola[10], G. Artaserse[1,11], L. Aucone[46], A. Augieri[11], F. Auriemma[43,54], J. Ayllon Guerola[50], N. Badodi[40], B. Baiocchi[6], L. Balbinot[51], C. Baldacchini[51], A. Balestri[46], T. Barberis[41], G. Barone[1,11], L. Barucca[2], M. Baruzzo[12], S. Begozzi[22], V. Belardi[48], F. Belli[11], A. Belpane[43], F. Beone[13], S. Bertolami[48], S. Bianucci[30], S. Bifaretti[48], S. Bigioni[22], W. Bin[6], P. Boccali[22], B. Boeswirth[34], E. Bogazzi[22], R. Bojoi[41], S. Bollanti[11], T. Bolzonella[43], F. Bombarda[48], M. Bonan[22], N. Bonanomi[6,34], A. Bonaventura[25], L. Boncagni[11], M. Bonesso[30], D. Bonfiglio[43,54], R. Bonifetto[41], D. Bonomi[42], D. Borgogno[9], T. Borzone[23], S. Botti[1,19], E. Boz[42], F. Braghin[40], M. Brena[20], S. Brezinsek[27], M. Brombin[43], A. Bruschi[6], S. Buonocore[10], P. Buratti[11], P. Buratti[48], D. Busi[40], G. Calabrò[51], M. Caldora[28], G. Calvo[41], G. Camera[10], G. Campana[23], S. Candela[30], V. Candela[30], F. Cani[51], L. Cantone[48], F. Capaldo[22], S. Cappello[43,54], M. Caponero[1,11], S. Carchella[1,19], A. Cardinali[9], D. Carnevale[48], L. Carraro[43], C. Carrelli[12], V. Casalegno[41], I. Casiraghi[6], C. Castaldo[11], A. Castaldo[11], G. Castro[31], A. Carpignano[41], F. Causa[6], R. Cavazzana[43], M. Cavedon[46], M. Cavenago[30], M. Cecchini[51], S. Ceccuzzi[1,11], G. Celentano[11], L. Celona[31], C. Centioli[11], G.V. Centomani[1,21], S. Cesaroni[11], A.G. Chiariello[10], R. Chomicz[23], C. Cianfarani[11], F. Cichocki[11], M. Cinque[10], A. Cioffi[10], M. Ciotti[1,11], M. Cipriani[11], S. Ciufo[43], V. Claps[11], G. Claps[10], V. Coccorese[10], D. Coccorese[10], A. Colangeli[11], T. Coltella[2], F. Consoli[11], F. Cordella[11], D. Corradini[42], O. Costa[36], F. Crea[11], A. Cremona[6], F. Crescenzi[11], F. Crisanti[1,51], G. Cristofari[11], G. Croci[46], A. Cucchiaro[1,16], D. D'Ambrosio[41], M. Dal Molin[6], M. Dalla Palma[43,54], F. Danè[1,22], C. Day[37], M. De Angeli[6], V. De Leo[11], R. De Luca[11], E. De Marchi[1,21], G. De Marzi[11], G. De Masi[43], E. De Nardi[43], C. De Piccoli[43,47], G. De Sano[1,48], M. De Santis[1,19], G. De Tommasi[10], A. Del Nevo[12], A. Delfino[51], A. Della Corte[10], P. Deodati[22], S. Desiderati[39], E. Di Ferdinando[11], M.G. Di Florio[24], G. Di Gironimo[10], L.E. Di Grazia[10], V. Di Marzo[10], F. Di Paolo[48], E. Di Pietro[1], M. Di Pietrantonio[51], M. Di Prinzio[2], A. Di Silvestre[19], A. Di Zenobio[11], R. Dima[30], A. Domenichelli[22], A. Doria[11], G. Dose[48], S. Dubbioso[10], S. Dulla[41], I. Duran[35], M. Eboli[12], M. Elitropi[42], E. Emanuelli[41], B. Esposito[11], P. Ettorre[1,16], C. Fabbri[1,22], F. Fabbri[15], M. Fadone[43], M.M. Faggiano[1,22], F. Falcioni[19], M.V. Falessi[11], F. Fanale[1,11], P. Fanelli[51], A. Fassina[11], A. Fassina[43], M. Favaretto[1,23], G. Favero[30], M. Ferraris[41], F. Ferrazza[20], C. Ferretti[1,20], A. Ferro[43], N. Ferron[43], C. Fiamozzi Zignani[11], L. Figini[6], F. Filippi[11], M. Filippini[23], A. Fimiani[10], M. Fincato[43], F. Fiorenza[10], D. Fiorucci[1,11], D. Flammini[11], F. Flora[11], N. Fonnesu[11], P. Franz[43], L. Frassinetti[38], A. Frattolillo[1,11], R. Freda[11], R. Fresa[10], A. Frescura[43], P. Frosi[11], M. Fulici[51], M. Furno Palumbo[1,11], V. Fusco[11],

[*] Author to whom any correspondence should be addressed.

P. Fusco[22], L. Gabellier[1,11], P. Gaetani[22], E. Gaio[43], E. Gajetti[41], P. Gaetani[56], A. Galatà[31], J. Galdon Quiroga[50], D.L. Galindo Huertas[41], S. Gammino[31], G. Gandolfo[15], S. Garavaglia[6], J. Garcia Lopez[50], M. Garcia Muñoz[50], P. Gaudio[48], M. Gelfusa[48], G. Gervasini[6], L. Giannini[11], M. Giarrusso[29], C. Gil[4], F. Giorgetti[1,11], E. Giovannozzi[11], G. Giruzzi[4], L. Giudicotti[43], M. Gobbin[43], G. Gorini[46], G. Granucci[1,6], D. Grasso[9], T. Grasso[23], S. Grazioso[10], H. Greuner[34], G. Griva[41], G. Grosso[6], S. Guerini[42], J.P. Gunn[4], V. Hauer[37], J. Hidalgo Salaverri[50], M. Hoppe[38], M. Houry[4], M. Hoelzl[34], A. Iaboni[21], M. Iafrati[11], A. Iaiunese[10], V. Imbriani[10], D. Indrigo[1,23], P. Innocente[1,43], F. Koechl[44], B. Končar[36], A. Kryzhanovskyy[43], L. Laguardia[6], D.A. Lampasi[1,11], C. Lanchi[1,11], F. Lanzotti[10], A. Lanzotti[10], M. Laquaniti[45], F. Leone[29,53], J. Li[3], M. Libè[1,11], F. Lisanti[41], D. Liuzza[52], F. Locati[22], R. Lombroni[51], R. Lorenzini[43], P. Lorusso[11], L. Lotto[43], J. Loureiro[43], F. Lucca[39], T. Luda Di Cortemiglia[34], P. Maccari[12], G. Maddaluno[11], S. Magagnino[11], G. Manca[48], A. Mancini[11], P. Mandalà[1,11], B. Mandolesi[48], F. Mandrile[41], G. Manduchi[43], S. Manfrin[43], M. Manganelli[1,11], P. Mantica[1,6], G. Marchiori[43], N. Marconato[43], G. Marelli[22], A. Mariani[6], A. Marin[39], R. Marinari[12], M. Marinelli[48], F. Marino[10], P. Marino[22], D. Marocco[11], R. Marsilio[41], E. Martelli[11], P. Martin[1,43], F. Martinelli[48], G. Martini[43], R. Martone[1,10], A. Marucci[51], D. Marzullo[10], V. Masala[22], D. Mascali[31], F. Mascari[16], A. Masi[11], N. Massanova[10], S. Mastrostefano[11], M. Mattei[10], G. Mauro[31], S. Mauro[41], C. Meineri[41], L. Melaragni[51], A. Mele[51], P. Meller[42], S. Meloni[51], I. Menicucci[11], G. Messina[1,11], L. Mezi[11], G. Miccichè[12], M. Micheletti[42], S. Migliori[1,11], D. Milanesio[41], F. Milazzo[22], R. Milazzo[43], P. Minelli[8], S. Minucci[51], F. Mirizzi[10], M. Missirlian[4], D. Monarca[51], C. Monti[11], M. Mori[23], A. Moriani[11], L. Morici[11], A. Moro[23], A. Moro[6], F. Moro[11], P. Mosetti[1,11], R. Mozzillo[10], A. Murari[1,43], A. Muraro[6], D. Murra[11], P. Muscente[43], S. Musumeci[41], L. Muzzi[11], G.F. Nallo[41], F. Napoli[11], E. Nardon[4], E. Naselli[31], R. Neu[34], M. Nocente[46], M. Notazio[51], S. Nowak[6], E. Ocello[43], A. Oliva[1,19], V. Orsetti[1,11], A. Orsini[30], F.P. Orsitto[11], M. Ortino[26], M. Ottavi[48,55], G. Paccagnella[23], D. Pacella[11], I. Pagani[39], N. Paganucci[23], A. Pagliaro[40], V. Palazzolo[23], M. Palermo[2], S. Palomba[1], F. Panza[11], D. Paoletti[1], M. Parisi[1,21], R. Pasqualotto[43], S. Passarello[31], M. Passoni[40], T. Patton[43], L. Pelliccia[17], A. Peloso[11], A. Pepato[30], E. Perelli[6], A. Perencin[22], S. Peruzzo[43], A. Pesenti[42], N. Pedroni[41], P. Petrolini[11], V. Piergotti[11], A. Pidatella[31], L. Pigatto[43], M. Pillon[11], T. Pinna[1,11], S. Pipolo[1,11], S. Piras[48], C. Piron[11], L. Piron[47], A. Pironti[10], M. Pistilli[11], D. Placido[41], A. Pizzuto[1], P. Platania[6], A. Polimadei[11], F. Pollastrone[11], G.M. Polli[1,11], N. Pomaro[43], F. Pompili[11], C. Ponti[49], F. Porcelli[41], V. Prandelli[42], A. Previti[11], A. Princiotta[22], G. Pucino[1,11], F. Quaglia[48], A. Quercia[10], F. Raffaelli[32], G. Ramogida[1,11], G. Ranieri[22], B. Raspante[11], D. Ravarotto[43], G.L. Ravera[11], A. Reale[1,11], P. Rebesan[30], M. Recchia[43], D. Regine[1], F. Renno[10], B. Riccardi[1], D. Ricci[6], D. Rigamonti[6], M. Ripani[33], N. Rispoli[6], S. Roccella[11], G. Rocchi[11], H. Roche[4], M. Romanato[30], F. Romanelli[6], F. Romanelli[1,48], G. Romanelli[51], R. Romaniello[1], A. Romano[1,11], M. Romano[21], R. Romano[1,11], R. Rossi[48], G. Rubinacci[10], G. Rubino[51], G. Rubino[8], S. Rubino[41], J. Rueda Rueda[50], A. Rufoloni[11], C. Salvia[47], P. Salvini[48], M. Scarpari[51], A. Salvitti[51], L. Salvò[30], S. Sandri[11], F. Santoro[43], A. Satriano[11], L. Savoldi[41], C. Scardino[1,11], G. Schettini[49], S. Schmuck[6], J. Scionti[6], M. Scisciò[11], M. Scungio[51], K. Sedlak[26], L. Senni[7], G. Sias[45], A. Sibio[11], A. Simonetto[6], L. Singh[41], A. Sirignano[1,19], C. Sozzi[6], I. Spada[5], S. Spagnolo[43], L. Spinicci[43], G. Spizzo[43], M. Spolaore[43], C. Stefanini[51], H. Strobel[37], F. Subba[41], F. Taccogna[8], B. Taheri[11], C. Tantos[37], A. Tarallo[10], M. Tarantino[16], G. Tardini[34], M. Tardocchi[6], P. Tarfila[36], A. Tenaglia[48], C. Terlizzi[48], D. Terranova[43], D. Testa[26], E. Testa[42], R. Testoni[41], V. Toigo[43], G. Torrisi[31], A. Trotta[1,21], G. Trovato[1,20], E. Tsitrone[4], A. Tuccillo[10], O. Tudisco[1,11], M. Turcato[30], S. Turtù[11], A. Uccello[6], M. Ugoletti[43], O. Uras[22], M. Uras[22], M. Utili[1,12], V. Vaccaro[1,11], F. Valentini[30], L. Valletti[48], M. Valisa[1,43], D. Van Eester[27], D. Vanzan[23], E. Vassallo[6], G. Vecchi[41], M. Vellucci[11], I. Venneri[25], G. Ventura[41], M. Veranda[43,54], L. Verdini[11], C. Verona[48],

G. Verona Rinati[48], F. Veronese[43], N. Vianello[43], F. Viganò[39], O. Villano[22], R. Villari[11], F. Villone[10], P. Vincenzi[43,54], V. Vitale[1,11], F. Vivio[48], G. Vlad[1,11], M. Wischmeier[34], H.S. Wu[41], I. Wyss[48], R. Zanino[41], B. Zaniol[43], F. Zanon[1,21], A. Zappatore[41], G. Zavarise[41], P. Zito[1,18], A. Zoppoli[10], M. Zucchetti[41], M. Zuin[43] and P. Zumbolo[10]

[1] DTT S.c. a r.l., via Enrico Fermi 45, 00044 Frascati, Roma, Italy
[2] Ansaldo Nucleare S.p.A., Via Nicola Lorenzi 8, 16152 Genova, Italy
[3] Institute of Plasma Physics, Chinese Academy of Sciences, Hefei 230031, China
[4] CEA, IRFM, F-13108 Saint Paul Lez Durance, France
[5] CETMA, S.S.7 Km.706+ 030, 72100 Brindisi, Italy
[6] ISTP-CNR, via R. Cozzi 53, 20125 Milano, Italy
[7] CNR IAC, Via dei Taurini 19, 00185 Roma, Italy
[8] CNR-ISTP, via Amendola 122/D, 70126 Bari, Italy
[9] CNR/ISC, Corso Duca degli Abruzzi 24, 10129 Torino, Italy
[10] Consorzio CREATE, Via Claudio 21, 80125 Napoli, Italy
[11] ENEA C. R. Frascati, via E. Fermi 45, 00044 Frascati, Italy
[12] ENEA, C.R. Brasimone, 40032 Camugnano, Italy
[13] ENEA, Lungotevere Thaon di Revel 76, 00186 Roma, Italy
[14] ENEA, Brindisi s.s. 7, km 706, 72100 Mesagne, Italy
[15] ENEA Casaccia, Via Anguillarese 301, 00123 Roma, Italy
[16] ENEA, Via Martiri di Monte Sole, 4 40129 Bologna, Italy
[17] ENEA, P.le Enrico Fermi 1, 80055 Portici, Italy
[18] ENEA Palermo, P.zza Ignazio Florio, 24, 90139 Palermo, Italy
[19] Eni, P.le Enrico Mattei 1, 00144 Roma, Italy
[20] Eni, Via Felice Maritano, 26, 20097 San Donato Milanese, Italy
[21] Eni, Via dell'Industria 39, 30175 Venezia, Italy
[22] Eni Progetti, Via Paride Stefanini, 11, 00144 Roma, Italy
[23] EniProgetti, Via dell'Industria 39, 30175 Venezia, Italy
[24] EniProgetti, Via Felice Maritano, 26, 20097 San Donato Milanese, Italy
[25] EniProgetti, Località Facciolo, 89900 Triparni, Vibo Valentia, Italy
[26] Ecole Polytechnique Fédérale de Lausanne (EPFL), Swiss Plasma Center (SPC), CH-1015 Lausanne, Switzerland
[27] Forschungszentrum Jülich GmbH, Institut für Energie- und Klimaforschung—Plasmaphysik, 52425 Jülich, Germany
[28] Sapienza Università di Roma, P.le Aldo Moro, 5, 00185 Roma, Italy
[29] INAF—Osservatorio Astrofisico di Catania, Via S. Sofia 78, I-95123 Catania, Italy
[30] INFN Sezione di Padova, Via Marzolo, 8, 35131 Padova, Italy
[31] INFN Laboratori Nazionali del Sud, Via S. Sofia, 62, 95126 Catania, Italy
[32] INFN Sezione di Pisa Largo Bruno Pontecorvo, 3, ed. C, 56127 Pisa, Italy
[33] INFN Sezione di Genova, Via Dodecaneso, 33, 16146 Genova, Italy
[34] Max-Planck-Institut für Plasmaphysik, D-85748 Garching, Germany
[35] IPP/CAS, Za Slovankou 1782/3, 182 00 Prague 8, Libeň, Czech Republic
[36] Jožef Stefan Institute, Jamova cesta 39, SI-1000 Ljubljana, Slovenia
[37] Karlsruhe Institute of Technology, PO Box 3640, D-76021 Karlsruhe, Germany
[38] KTH, SE-10691 Stockholm, Sweden
[39] LTCALCOLI, Via Bergamo, 60, 23807 Merate, Italy
[40] Politecnico di Milano, P.zza Leonardo da Vinci, 32, 20133 Milano, Italy
[41] Politecnico di Torino, Corso Duca degli Abruzzi 24, I-10129 Torino, Italy
[42] PROMECH, Via XXV Aprile 1945, 38, 24050 Zanica, Italy
[43] Consorzio RFX, corso Stati Uniti 4, 35127 Padova, Italy
[44] UKAEA Culham Science Centre, Culham OX14 3DB, United Kingdom of Great Britain and Northern Ireland
[45] Department of Electrical and Electronic Engineering, University of Cagliari, Piazza d'Armi 09123, Cagliari, Italy
[46] Università degli Studi di Milano-Bicocca, piazza della Scienza 3, 20126 Milano, Italy
[47] Università degli Studi di Padova, Via 8 febbraio, 2, 35122 Padova, Italy
[48] Università di Roma Tor Vergata, Via del Politecnico 1, Roma, Italy

[49] Department of Industrial, Electronic and Mechanical Engineering, Roma Tre University, via Vito Volterra 62, 00146 Roma, Italy
[50] Universidad de Sevilla, C. San Fernando, 4, 41004 Sevilla, Spain
[51] University of Tuscia, DEIM, Via del Paradiso 47, 01100 Viterbo, Italy
[52] Università del Sannio, Via Traiano, 3, 82100 Benevento, Italy
[53] Dipartimento di Fisica e Astronomia, Sezione Astrofisica, Università di Catania, Via S. Sofia 78, I-95123 Catania, Italy
[54] ISTP-CNR, Corso Stati Uniti, 4, 35127 Padova, Italy
[55] University of Twente, Enschede, Netherlands
[56] Rina consulting SpA, Via Cecchi 6, 16129 Genova, Italy

E-mail: francesco.romanelli@dtt-project.it

Received 11 January 2024, revised 3 June 2024
Accepted for publication 12 June 2024
Published 11 September 2024

Abstract

An overview is presented of the progress since 2021 in the construction and scientific programme preparation of the Divertor Tokamak Test (DTT) facility. Licensing for building construction has been granted at the end of 2021. Licensing for Cat. A radiologic source has been also granted in 2022. The construction of the toroidal field magnet system is progressing. The prototype of the 170 GHz gyrotron has been produced and it is now under test on the FALCON facility. The design of the vacuum vessel, the poloidal field coils and the civil infrastructures has been completed. The shape of the first DTT divertor has been agreed with EUROfusion to test different plasma and exhaust scenarios: single null, double null, X-divertor and negative triangularity plasmas. A detailed research plan is being elaborated with the involvement of the EUROfusion laboratories.

Keywords: divertor, exhaust, plasma scenarios

(Some figures may appear in colour only in the online journal)

1. Introduction

As pointed out by the 'European Research Roadmap to the Realization of Fusion Energy' [1, 2], the heat exhaust is one of the main challenges towards the construction of a fusion power plant. For this reason, a dedicated Divertor Tokamak Test (DTT) facility was considered necessary. In order to address this challenge, a high-field, compact tokamak design (table 1) [3] was proposed capable of producing plasma conditions similar to those in ITER and DEMO in steady–state conditions and, thanks to a substantial amount of external heating power (up to 45 MW to the plasma), to reproduce the level of divertor heat loads foreseen in ITER and DEMO. Flexibility is a primary requirement for DTT. The machine is expected to explore a variety of different magnetic configurations and in extreme conditions (high heat-flux, large electromagnetic loads) while guaranteeing high reliability and availability with 100 operation days per year. The DTT scientific programme will be articulated along four main lines of investigation: (a) magnetic configurations that allow large divertor wetted areas and detached plasma conditions; (b) advanced plasma facing components technology; (c) impurity seeding to increase core radiation; and (d) liquid metals as plasma facing component. These research lines will aim at identifying and qualifying integrated core-edge solutions i.e. regimes with simultaneously high-radiated fraction and good confinement. DTT will be the only breakeven-class device in the world equipped with full tungsten actively cooled components before ITER. The recent decision of ITER to switch to full-tungsten first wall (FW) makes DTT an ideal tool to test plasma scenarios and engineering solution in advance of their implementation on ITER.

Calculations of the equivalent Q_{DT} for the simulation of the baseline full power scenario shown in figure 1 indicates values in the range $Q_{\mathrm{DT}} = 0.3$.

This paper provides an overview on the state of the construction, with particular attention to the elements of originality of the design, and of the preparation of the research program.

The challenges for the DTT design come mainly from the high toroidal magnetic field, wide range of plasma shaping, central solenoid (CS) flux swing requirements for 5.5 MA/100 s pulses, need to exhaust heat fluxes in excess of 20 MW m^{-2}, need to inject up to 45 MW of additional heating power (a level of power comparable with that foreseen in ITER and DEMO) in a compact device [4].

The toroidal field (TF) coils have been designed using the recent advances in superconducting strand technology to meet the requirements of high magnetic field and to maximize the available magnetic flux generated by the CS to allow

Table 1. DTT parameters.

R (m)	a (m)	B_t (T)	I_p (MA)	P (MW) (ECRH/NBI/ICRH)	t_{pulse} (s)
2.19	0.70	5.85	5.5	45 (28.8/9.5/6.7)	100

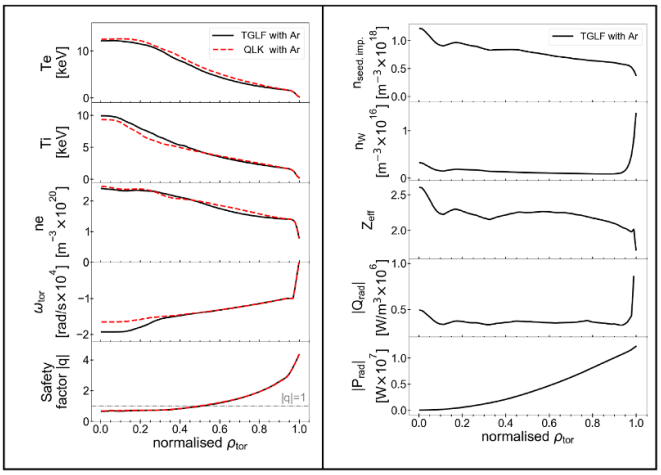

Figure 1. Radial profiles for the full power scenario flat-top phase with argon seeding: (left) electron and ion temperatures, electron density, toroidal rotation, and safety factor absolute value, with turbulent transport calculated by TGLF SAT2 (solid black lines) or by QLK (dashed red lines); (right) profiles of the seeding impurity and tungsten densities, effective charge, radiative power density, and radiative power, calculated by TGLF and FACIT. Reproduced from [12].

long-pulse inductive operation. The critical current of the DTT Nb_3Sn strand (for the TF coils) is 320 A and has been tested in the Sultan facility showing an excellent performance with the temperature margin, remaining unchanged after 3000 cycles. The DTT CS has to produce a flux swing in excess of 16.2 Wb, with a bore radius of less than 0.8 m. Two different solutions have been analysed (a layer-wound solution and a conventional double pancake) to find the best trade-off between flux production and fabrication risks, considering both electric and mechanical issues. The strand for the DTT CS also requires a critical current larger than that of the ITER CS and very low AC losses. The DTT CS conductors will be submitted to an extensive test at Sultan facility.

DTT plasma facing components require particular care in design and fabrication to ensure the achievement of the machine goals. The divertor region must be compatible with different divertor concepts and technologies including liquid metals. Present plans aims at using capillary porous systems with tin as liquid metal. The divertor volume has to ensure an efficient pumping and the possibility to operate at DEMO relevant conditions (pressure up to 15 MPa and cooling temperature up to 250 °C). The shape of the plasma facing units (PFUs) has been optimized to be compatible with single null (SN), X-Divertor (XD) and negative triangularity (NT) scenarios, through extensive analyses of the neutral pressure at the sub-divertor region as well as temperature and stresses. The FW has been conceived with a large area capable to operate as limiter with 18 out of 36 inner FW panels made of tungsten monoblocks and the others made of stainless steel coated with W. The solid tungsten armoured inner FW has been designed to withstand a heat flux in excess of 10 MW m^{-2} and to guarantee suitable flexibility during plasma ramp up. The DTT FW will be provided with passive protection against runaway electrons. The system is currently under design. The expected maximum heat flux due to radiation impinging on the wall is about 0.5 MW m^{-2}. The water-cooling distribution has been designed to be fully compatible with remote handling (RH), including cutting and welding tooling for tubes and manifolds.

Extensive structural analyses of the vacuum vessel (VV) have been carried out considering the most demanding combination of events [5] (disruptions, earthquake). To limit the neutron heating in the TF coils, the VV cooling channels will be eventually filled with borated water. The VV is a critical component for the design of all the Plasma Facing Components. In fact, to prevent FW misalignment and to guarantee the proper plasma FW distance, very tight fabrication tolerances must be achieved for the VV that are challenging as the DTT VV consists in a fully welded double wall 15 mm thick structure made of AISI 316 LN steel. The VV will be equipped with about one thousand of sensors for magnetic diagnostics and machine protection.

Also, in the area of additional heating DTT is bringing innovative solutions. The 32 MW electron cyclotron heating (ECH) will be transmitted by means of vacuum lines to limit the power losses—a DEMO relevant solution. The mirrors, which will operate at high temperature (190 °C for the launcher mirror), require real time steering at high speed (20° s^{-1} for the launcher mirror). Mirrors will be fabricated with unconventional technology. Prototypes by additive manufacturing have been already produced while the possibility to use ceramic materials is under study. The opportunity to realize a test bed for testing and calibrating the system is under evaluation. The ion cyclotron heating (ICH) power units will be based on an innovative solid-state system. To allow the injection of at least 1.5 MW per port, the antenna, being larger than the port area, has to be assembled inside the VV by RH. The design of the 510 keV/10 MW negative ion based neutral beam injector (NBI) is made challenging by the presence of significant magnetic fields around the tokamak and by the high-power density. In order to improve the beam efficiency and reduce losses, the accelerator is made by additive manufacturing. To prevent unacceptable losses, the injector is magnetically shielded. The NBI shielding has been designed to avoid introducing error fields in the plasma region.

Since 2021, a number of important milestones have been achieved for the licensing and permitting procedures. The licensing for ‘Category A ionizing radiation source’ has been granted to ENEA in March 2022 by the Italian Ministry for Ecologic Transition. The production of radiological waste has been evaluated and suitable temporary storage is foreseen. A hot cell will be utilised for separating the material according to their decay time in order to make their disposal faster. The approval for the construction of the new buildings (about 150.000 m^3) has been granted by the Italian Ministry

of Infrastructures and Sustainable Mobility and by the local authorities at the end of 2021. The definitive design of the 150 kV line connecting the Rome east node with the Frascati laboratory has been approved by the Italian Ministry of Environment and Energy Security in January 2023. The connection will be entirely financed by the Italian Transmission System Operator TERNA as part of the general plan for the upgrade of the electric network. On site civil works have been delayed by the discovery of beryllium concentration slightly above the limit. This has requested an additional procedure to identify the potential risks. The procedure was successfully concluded in June 2023.

Since 2021, the set of possible configurations to be investigated by DTT has been enlarged and assessed in interaction with EUROfusion in order to meet the scientific needs of the Euratom programme. Already in the first phase of exploitation, DTT will be capable of demonstrating, in addition to the conventional SN scenario, also the XD, double null (DN) and NT configurations with a maximum plasma current up to 5.5 MA (SN), 4.5 MA (XD), 4 MA (DN and NT). On the basis of this analysis the design of the first DTT divertor has been agreed with EUROfusion in 2022. This increase of the scope of the project had an impact on the design of the VV that had to be slightly enlarged. Furthermore, a set of 3D in-vessel coils (3 rows/9 coils per row) for ELM control and error field compensation was inserted.

To construct and operate the DTT facility a company named DTT S.c. a r.l. has been set up in 2019. The central team has increased from 10 to about 80 professionals. Most of the design activity is made through specific tasks assigned to the DTT shareholders and through external engineering services. The design maturity has progressed significantly.

The construction of the machine is progressing with about one third of the total budget being committed in running industrial contracts. The 18 TF coils and the related power supplies and protection system are in the manufacturing stage. The framework contract for the procurement of 16 gyrotrons has been signed in 2021. The pre-series gyrotron has been manufactured and has been successfully tested in the FALCON facility. The call for tender for the ICRH solid state transmitters, launched as part of the DTT-U PNRR project financed under the Next Generation EU programme, has been assigned. The definitive design of the new buildings has been completed and the design of the electrical distribution system (including the new 150 kV/20 kV switchyard) is near completion. The call for tender for these two items will be launched, after an independent verification foreseen by the Italian law, in 2024.

In the last two years a review of the cost and schedule has been performed. The lifetime plan is periodically updated. Funds for 614 M€ have been secured by ENEA. The target for first plasma operation is 2029.

2. Physics basis

In the international frame of fusion research, the DTT represents the main European facility where to test innovative techniques for the treatment of plasma exhaust and for the study of possible divertor concepts in ITER-like and DEMO-relevant conditions.

The main challenge faced by DTT is to create, albeit on a reduced geometrical size, functional conditions similar to those of ITER and DEMO.

In this section the physical models underlying the project are illustrated, with particular reference to the scenarios foreseen for operations, the key issues of power exhaust and the most critical aspects of the expected instabilities.

2.1. DTT reference plasma scenarios

A key tool for the design of a magnetic confinement fusion device is the first principle based integrated modelling of the plasma scenarios, which allows to predict plasma performance and therefore to optimize machine design and reduce risk, plan for control systems, design diagnostics and set the basis for the future physics studies. A key requirement for the integrated modelling of the DTT plasma scenarios is that of enforcing coherence between high performance plasma core and scrape-off layer (SOL) parameters consistent with divertor plasma detachment, assuming to radiate about 30% of the power within the boundary set by the separatrix, by means of the seeding of light impurities.

To this extent, DTT modelling has been realized using the codes JINTRAC [6] and ASTRA [7] with the support of the transport models TGLF [8] and QuaLiKiz [9] and, in addition, the pedestal model EPED; the analyses provide temperatures, density, current density, rotation and two impurity densities (W plus either Ar or Ne) up to the plasma separatrix [10]. SOL simulations have been realized with the SOLEDGE2D-EIRENE code which couples a fluid treatment for plasma with a kinetic one for the neutral dynamics [11]. This approach allows to explore the edge plasma from $\rho_{\rm tor} = 0.85$ (i.e. just inside the pedestal top) up to the FW.

Both, full power and reduced power scenarios in lower SN configuration have been simulated, the latter with magnetic field and current values that will characterize the early phases of operations. At full power, the plasma current is $I_{\rm p} = 5.5$ MA and the toroidal magnetic field $B_{\rm t} = 5.85$ T, with the following heating mix: (a) for ECH 32 gyrotrons to provide approximately 28.8 MW in O-mode to the plasma, (b) for ICH 4 radiofrequency (RF) antennas split in 2 modules, which deliver a total power to the plasma of about 6.0 MW; (c) for NBI, one negative ion beam at 510 keV which provides 10 MW to the plasma.

The radial profiles of electron temperature $T_{\rm e}$, ion temperature $T_{\rm i}$, electron density $n_{\rm e}$, toroidal rotation $\omega_{\rm tor}$, safety factor absolute value $|q|$, seeding impurity density $n_{\rm seed.imp.}$, tungsten density $n_{\rm W}$, effective charge $Z_{\rm eff,}$ radiative power density $Q_{\rm rad}$, and radiative power $P_{\rm rad}$ (emitted up to a radius ρ) obtained by the two simulations with Ar as seeding gas and with the turbulent transport models of TGLF or QLK for the full power scenario are shown in figure 1, from [12]. The neoclassical transport of impurities has been calculated by the FACIT model [13], whilst NCLASS [14] was used for the main species.

The temperature profiles obtained with the two models are in good agreement. The electron temperature is larger than the

ion temperature over almost all plasma radii. Despite the high thermal exchange power from electrons to ions, the ion temperature profile is limited because the ion temperature gradient mode (ITG) threshold is low for $T_e/T_i > 1$ and a strong ion stiffness is predicted by the turbulent transport model. This scenario is indeed dominated by the ITG modes over most of the radial profile. Impurities do not accumulate significantly in the plasma centre.

To operate the scenarios at full power with high density a suitable fuelling is required; pellets ($r = 1$ mm) injected obliquely, from the high field (HF) side, with a velocity of 516 m s^{-1} and a frequency in the order of 10–20 Hz are expected to be able to guarantee the desired density profile, provided the ECH deposition is rather broad as described in [12, 15].

Simulations of the time history during the full discharge, carried out by means of ASTRA/TGLF/IMEP [16] demonstrate that the present CS design allows for reaching nominal plasma current values with a flat-top duration of 30–40 s, sufficient for physics studies.

DTT will be in ideal position to test disruption mitigation systems in advance of ITER. Analyses carried out with MAXFEA for various disruption mechanisms followed by electromagnetic analysis using ANSYS followed by the mechanical stress analysis using ABAQUS and including the effect of halo currents show that even in the worse scenario the VV satisfies the ASME-VIII stress requirements considering a fatigue life of 750 worse case disruptions (downward vertical displacement event at 5.5 MA) and of 2000 of lower severity disruptions

2.2. MHD stability analysis

Both, full power and reduced field and current scenarios have been analysed by means of ideal as well as resistive (low-n) MHD stability approaches.

Resistive stability analyses have been performed using the MARS code, applied to steady state plasma scenarios coming from transport simulations [17].

As expected, inside the $q = 1$ surface in the plasma region, an internal unstable kink has been localized (figure 2(a) from [17]). In this analysis, it is supposed that the conducting wall is far from the plasma boundary. The value of r_{ext} (normalized distance defined as the wall minor radius normalized on the plasma minor radius) has been fixed to $r_{ext} = 3$.

Figure 2(b), describes the dependence of the normalized growth rate γ, on the wall distance r_{ext}: it demonstrates an internal mode is dominant, although the dependence of the growth rate from the wall position implies the presence of an external mode component as well. Such a large $q = 1$ radius is detrimental because the internal kink causes large sawtooth crashes which could trigger NTMs. Indeed, sawteeth with a frequency ∼1.4 Hz with a drop of the central temperature by 44% are predicted in the inner half of the high current plasmas in DTT (figure 3, of [10]), using the Porcelli model [18] and Kadomtsev reconnection model [19] integrated in the JINTRAC suite. Further integrated modelling is ongoing

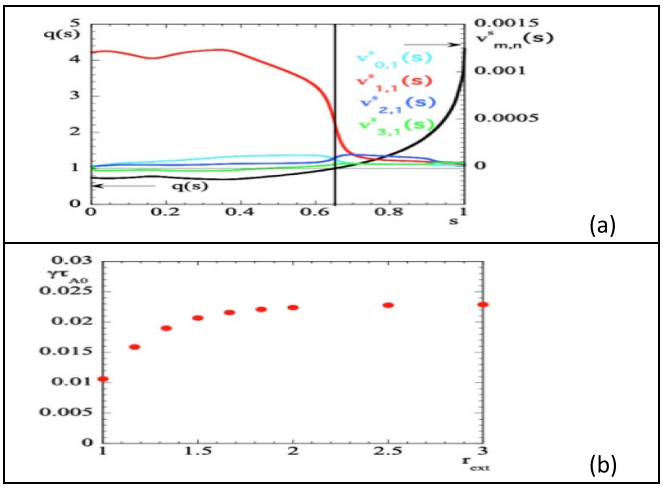

Figure 2. Stability characteristics. (a) Dominant contravariant Fourier components of the perturbed velocity $v^s_{m,n}$ for the internal kink mode safety factor q versus s (where $s \sim (\text{psi})^{1/2}$ is the normalized radial-like coordinate, and psi the poloidal flux function) at $r_{ext} = 3$. (b) Internal kink growth rate, normalized to the inverse of the on axis Alfvèn time τ_{A0} ($\tau_{A0} = R_0(\mu_0\rho_0)^{1/2}/B_0$), ρ_0 is the on axis mass density) versus the normalized distance r_{ext} of the perfectly conducting wall. Reproduced with permission from [17].

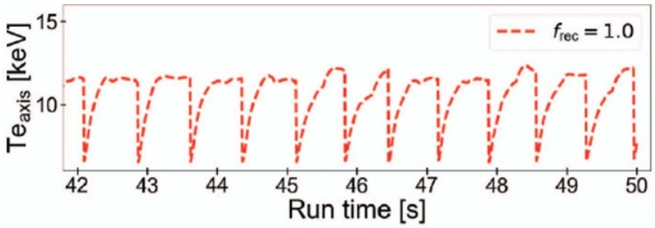

Figure 3. Time evolution of the electron temperature at the plasma centre, using the complete Kadomtsev reconnection model. Reproduced from [10]. © The Author(s). Published by IOP Publishing Ltd. CC BY 4.0.

to optimize control of sawteeth with the available heating and current drive capabilities. Also, the operation at higher q_{95} as in hybrid scenarios is foreseen for DTT and will be object of future integrated modelling work.

Due to the simultaneous action of different additional heating systems, the presence of energetic particles (EPs) is expected. The impact of EP is crucial from several points of views.

The possible damage of the plasma facing components due to the EP losses has been investigated by means of ORBIT [20] and ASCOT codes [21].

In particular the losses stemming from fast ions trapped by the magnetic ripple have been evaluated by means of ORBIT simulation and their impact has been minimized by suitably adjusting the NBI injection angle and the energy.

The NBI sources have been realistically modelled by the ASCOT code, including the 3D beam divergence and the EP tracking. The aim was the analysis of both losses and confinement mechanisms [21].

Also, the possible increment of EP losses due to the interaction with Alfven Eigenmodes has been analysed by means of a kinetic analysis [22]. DTT will be capable of independently control the parallel component of the fast particle population (through NBI) and the perpendicular component (through minority ICH) making it an ideal tool to test fast particle physics.

2.3. Power exhaust in different divertor configuration

The performance of the divertor in various configurations feasible in DTT has been analysed and compared by using SOLPS-ITER and SOLEDGE2D-EIRENE codes to model the plasma exhaust process. Specifically, the standard SN and the alternative XD (including the long legs variants) have been considered as well as the NT configuration. The study also included the compatibility analysis of the divertor shape. Two different radiating impurities, neon and argon, were tested in the high-power scenario to evaluate the minimum impurity concentration required to achieve sustainable conditions at DTT divertor. The sensitivity of the model was studied by varying the impurity concentration. Simulations of DTT maximum input power single-null scenario prove that this scenario can be operated obtaining sustainable power flux and temperature at both inner and outer divertor targets with both Ne and Ar seeding with acceptable $<Z_{\rm eff}>_{\rm sep}$, with Ar providing better cooling efficiency and higher radiated power fraction.

Hysteresis-like behaviour was observed during the scan on impurity gas-puffing [23], with the transition from attached to detached plasmas requiring more gas puffing than the reverse process. This non-linear dependence on impurity content is not specific to DTT but when compared to present experiments like JET and ASDEX the modelling results shows a more pronounced hysteretic behaviour. The reason of this enhanced non-linearity is probably the very high value of the ($BP_{\rm SOL}/R$) parameter in DTT at full power which, in order to access detached conditions, requires to dissipate a larger amount of power by radiation in a narrow volume. It will be part of future experiments to verify the impact on the development of the time evolution of plasma scenario.

The study provided also further useful indication. In the full power operation, the achievement of a low plasma temperature at the targets for reducing tungsten influx is a more stringent condition than the requirement of operating below the power load limit of 20 MW m^{-2} imposed by tungsten divertor monoblocks performance. In the initial phases DTT will operate at reduced plasma current and TF. In these conditions the detached state is more likely, because the expected longer heat flux decay length at lower magnetic field predicted by the Eich scaling [24] indicates a higher perpendicular heat in the SOL.

Power exhaust modelling [11] has contributed to the analysis of different divertor shapes compatible with engineering constraints and functional requirements on alternative divertor configurations and to the definition of the initial DTT divertor.

Modelling activity has shown the clear advantage of a wide divertor (a divertor with a larger separation between vertical targets) in respect to a narrow one with the same grazing angle at divertor targets. The wide divertor provides better performance for the standard SN configuration in all plasma conditions analysed, allowing for the same separatrix plasma density detached condition at: (a) higher power in pure deuterium; (b) lower $<Z_{\rm eff}>_{\rm sep}$ and impurity content with seeding at full power. This is due to the longer length of the legs and the closure provided by the vertical targets since the angle in the poloidal plane between the legs and vertical targets is smaller in the wide divertor providing a better closure for neutrals emitted at the targets. The wide divertor has been partially improved with the flat dome also for the XD configuration, although the XD configuration performs slightly worse than the SN in the code. The wide divertor allows also testing long legs configurations, which from the present analysis provide performance similar to the SN. Figure 4, taken from [11] shows some candidate divertor shapes, which have been studied.

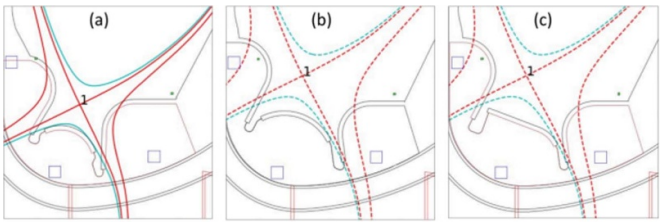

Figure 4. Examples of divertor shape under evaluation: (*a*) narrow divertor, (*b*) wide divertor, (*c*) wide divertor with flat dome. Reprinted from [11], Copyright (2022), with permission from Elsevier.

Mainly related to the allowed minimum radius of curvature of targets and the need to protect cooling pipes from parallel heat flux, the present modelling assisted design has shown that available tungsten monoblocks technology sets strong limitations on divertor shape for a divertor able to sustain high heat flux. This affects in particular alternative configurations like the XD. On one side this could be seen as a limitation of the designed divertor but on the other side it provides a realistic test bed for alternative divertor configurations directly scalable to DEMO. Additionally, it has to be noted that further optimizations are still possible both on the divertor side for which a longer external target is presently under evaluation and in terms of possible optimization in magnetic configurations.

An example of a partially detached scenario with Ar seeding for the finally selected divertor shape is shown in figure 5. The high electron density (figure 5(*a*)) at the divertor legs and at the targets produces a plasma detachment localized to the target regions (figure 5(*b*)), consequently the neutral pressure is also very high at the strike points (figure 5(*c*)). Following the density distribution, the total radiation is confined in the divertor along the legs (figure 5(*d*)). The variation of neutral pressure at the two main pump apertures (at the corners between the dome and the vertical targets) is particularly important for the pump design, so it has been calculated with different degrees of detachment. For the designed pumping speed of 100 $m^3\ s^{-1}$ a flow rate in the range $5 \cdot 10^{22}$–$15 \cdot 10^{22}$ D s^{-1} has been obtained, with the highest values corresponding to the partially detached condition like the case in figure 5.

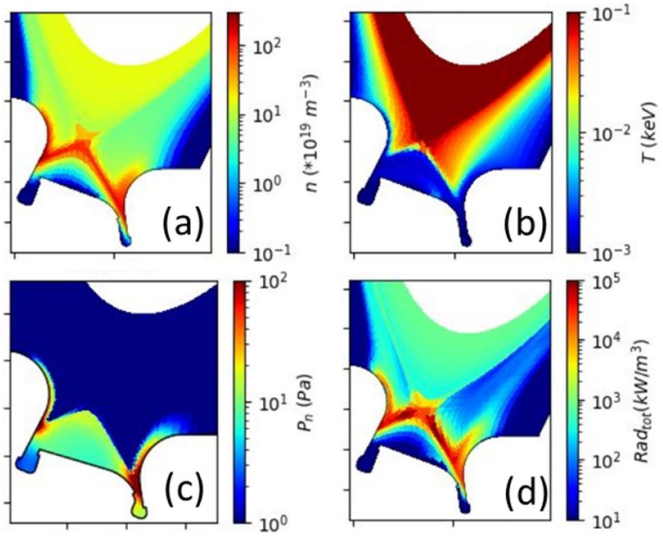

Figure 5. Examples of detached scenario with Ar in the divertor region: (a) electron density, (b) electron temperature, (c) neutrals ($D + D_2$) pressure, (d) total radiation.

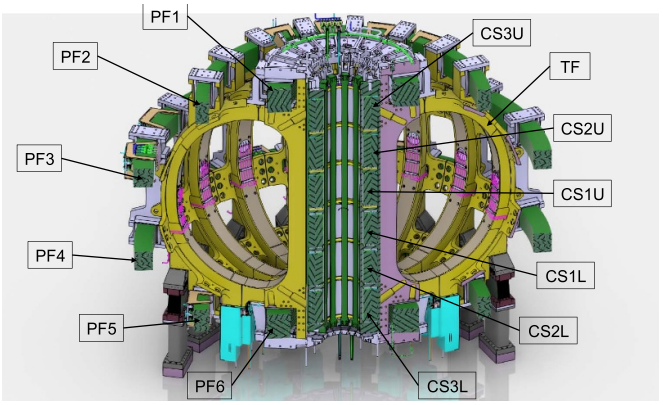

Figure 6. Schematic view of the magnetic system. Reproduced with permission from DTT team.

3. Tokamak components

3.1. Superconducting magnet system

The magnet system of DTT is based on three groups of superconducting coils: the 18 TF ones, providing a magnetic field of 5.85 T at the plasma axis; 6 external poloidal field (PF) ones, providing plasma shaping and stabilization; a stack of 6 identical modules for the CS, which are independently fed to provide a double flux swing of about 32.4 Wb [25]. In figure 6 a schematic view of the magnetic system is reported.

In order to reach the foreseen performances, the TF, the CS and the PF1 and PF6 coil pair (located at the polar region of the tokamak) have been designed with Nb_3Sn strands, whereas the other 4 PF coils rely on NbTi, as they operate at lower magnetic field. The technology of cable-in-conduit conductors (CICCs), cooled down by a forced flow of supercritical He gas having an inlet temperature of 4.5 K, has been chosen for its intrinsic high structural capability.

All the PF and CS coils loads are supported by the TF coils through specific supports, though they are all free to make relative radial movements. The weight of the superconducting feeders, the busbars portion which is internal to the machine cryostat and that works at cryogenic temperature, is also partially loaded to the TF structure.

3.1.1. TF coils system. The fabrication of the 18 TF coils is ongoing through three different procurement contracts: (i) TF conductor; (ii) winding pack (WP) and integration into the casing; (iii) casing structure. The coils are wound in pancake configuration and rely on 3 Double Pancakes named 'regular', placed in the centre of the WP, plus 2 'side' shorter Double Pancakes. All the coils are fed, with a current of 42.5 kA, in series, but they are discharged in 3 groups of 6 coils each, in order to limit the maximum voltage. Each pancake is cooled by a flow of 4 g s^{-1} of He at 4.5 K that insures a temperature margin on the conductor of about 1 K. The maximum magnetic field (11.9 T) is experienced in the inner leg at the equatorial plane [26].

Each TF WP is enclosed in an AISI 316LN SS casing, for structural reinforcement. The casings act also as supports, through dedicated frames, for the 6 PF coils, the CS stack and for part of the weight of the feeders. Each TF casing transfers its weight over a Gravity Support, where a series of laminated plates allow for the magnets radial displacements, impeding the toroidal ones.

On each side of the casings a pair of two cooling channels provides assistance to the magnet cool-down from room temperature but also to absorb the nuclear heating coming from the plasma during the discharge. Between the WP and the casing, a nominal 4 mm gap is foreseen for the integration activity into the casing. This gap will be filled during the so-called embedding operation in order to guarantee the load transfer from the WP to the casing during the energisation of the magnet [27].

All the TF coils casings are mechanically linked by a set of different inner and outer inter-coil structures, blocked by means of bolts, pins and custom-designed pieces. The gravity supports, made of laminated plates to allow radial movement due to thermal contraction of the TF system, are equipped with a 'thermal anchor', constituted by a cooling channel in which He flows at 4.5 K, in order to absorb the heat entering by conduction from the cryostat in the TF.

To better understand the challenge that the DTT TF coils system project represents, table 2 compares the DTT TF coils performances with those of ITER and JT-60SA. In table 2 ε_{appl} is the value of the applied strain at which the strand performance is measured (irrelevant for a NbTi strand). Figure 7 shows a render image of the 18 TF coils modules.

3.1.2. PF coil system. The PF coil system includes 6 solenoids, almost identical in pairs. Each coil is separately and independently fed. All PF coils are designed to be wound with pancake technique. The procurement of these coils has not yet been launched, nonetheless the call for tender is expected soon

Table 2. Comparison of DTT with ITER and JT-60SA performances.

	DTT	ITER	JT-60SA
Strand type	Nb_3Sn	Nb_3Sn	NbTi
Min. Critical current (specification)	320 A (4.2 K; 12 T; 0% ε_{appl}) (<1000 mJ cm^{-3} hysteresis losses)	190 A (4.2 K; 12 T; 0% ε_{appl}) (<500 mJ cm^{-3} hysteresis losses)	200 A (4.2 K; 8 T) (<500 mJ cm^{-3} hysteresis losses)
Engineering current density (MA m^{-2})	∼28	∼11	∼18
Stored magnetic energy (GJ)	2.5	41	1.05
Vertical force per half coil (MN)	30	205	9

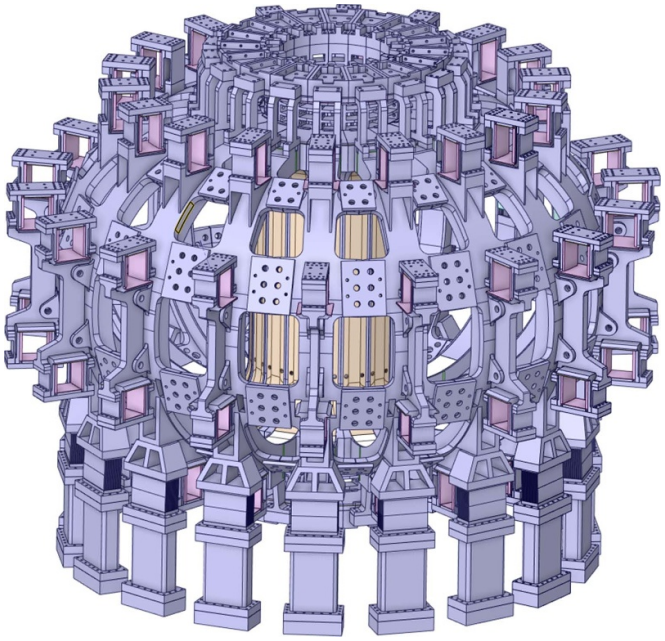

Figure 7. DTT TF magnet assembly. Reproduced with permission from DTT team.

since the PF6, PF5 and PF4, the lowermost coils in the tokamak, need to be placed on the base of the cryostat before starting with the assembly of the TF and the VV.

The most performing coils of the PF system are the PF1–PF6 pair. They have to operate at a maximum field of about 9.1 T with a maximum current of 28.3 kA, thus their design is based on a **Nb_3Sn** CICC. The CICC has a rectangular shape geometry, with constant thickness steel jacket and either very short twist pitch cable configuration or long twist pitch and low void fraction. The CICC option will be chosen after conductor qualification phase. Also, the assumption of $\varepsilon_{eff} = -0.65\%$ for the **Nb_3Sn** strand has been made.

The other two solenoid pairs (PF2–PF5 and PF3–PF4—see figure 6) operate at much lower magnetic field, so they can be based on less performing NbTi superconducting strand, but relying on CICC conductor and pancake winding technology as for the PF1/6 coils.

Given the hydraulic length, for all PF coils the presence of a central channel inside CICC is foreseen, to relief pressure drop between liquid He coolant inlet and outlet. It is worth noting that, due to their size, the transportation of PF3 and PF4 to DTT site will require a special logistic arrangement [28].

3.1.3. CS system. The CS is constituted of six stacked Nb_3Sn independent modules, enclosed within a steel axial precompression structure. The weight of the CS system is loaded at the bottom through its support to the TF coils casing. The magnetic hoop forces during operation are reacted internally, within the winding, by the conductor jacket. As the six modules are separately fed, the CS is able not only to induce the current inside the plasma, but also to shape it. Winding solutions based on either pancake- or layer-winding have been thoroughly investigated, to identify advantages and disadvantages, and make a final choice with minimized manufacturing and operational risks. In case of layer-winding, two submodules are foreseen, a HF and a low field one, made of a different rectangular CICC optimized for the specific operating values of magnetic field and current density, and connected through an external inter-layer joint. In case of pancake winding, a coil solution has been defined trying to minimize the coil operating current, and thus the CICC size, as well as its aspect ratio, so as to reduce the risks due to coil handling after the Nb_3Sn reaction heat treatment, for the application of the inter-turn insulation [29].

3.2. Power supply system

Strictly related to the superconducting magnet system is the power supply system. It includes the power supply for the superconducting magnets, with the protection and busbar, as well as the power supply for the in-vessel coils.

The procurement of both the TF coils power supply and the three fast discharge units is progressing well and the first delivery will be installed in the ENEA cold test facility for the test of the DTT coils. Call for tenders related to PF coil and CS systems will follow those of the corresponding magnet systems.

Additional (in-vessel) coils are included in the DTT design. Five of them are axisymmetric: two devoted to stabilize

plasma, the other three, located under the divertor, to the fine control of the X-point. In addition, a set of 27 non-axisymmetric coils, devoted to control ELM events and to the error field correction (EFC), is also foreseen. For the power supply system several different innovative solutions were proposed:

- The 18 TF coils are supplied in series by a 44 kA AC/DC converter, implementing a 24 pulse topology to reduce the harmonic contents at the input and the current ripple at the output [30]. The maximum TF ripple at the separatrix in SN operation is 0.6%.
- The fast discharge units and the switching network units (SNUs) are implemented by fully-static redundant switches [30].
- The energy stored in the superconducting coils is discharged by high-energy SiC varistors instead of standard resistors [30, 31]. This allows an optimized trade-off between the discharge time, the energy passing through the coils and the peak voltage [31].
- The 6 CS modules are supplied by 6 independent 1 kV 32 kA IGBT-based H-bridges [30]. In each CS circuit, both the breakdown overvoltage and the emergency protection are implemented by a fully-static SNU containing banks of high-energy SiC varistors [30].
- The 6 PF coils are also based on energy storage and H-bridges, but the voltage is much higher (2 kV or 3 kV) also because the breakdown voltage is generated without a SNU [30].
- Most of pulsed power supplies adopt energy-conservation topologies introducing large supercapacitor banks in the DC-links (distributed energy storage) [30]. Ideally, the energy in the coil circuit is conserved (only transformed from an electrostatic to a magnetic form) and recovered after a pulse for a new operation. This limits the input power to a small percentage of the required output power to the load coils.
- The same couple of anti-series in-vessel coils, supplied by a common circuit of fast converters with an additional imbalance branch, are able to implement both the vertical stabilization and radial control functions, with a mitigated effect of the plasma disruptions [32].

3.3. Vessel, in-vessel and out-vessel components

In DTT, the plasma will be contained in a D-shaped VV characterized by a double wall structure to provide high rigidity against operational load and high toroidal one-turn resistance (figure 8). The VV overall mass including ports, bellows, and gravity supports is about 174 ton plus 14 ton of coolant. The assembly is about 9.5 m high with about 11.5 m diameter. Each gravity support is made of a vertical leg and is laid on the ring pedestal through a pack of spring plates to accommodate free thermal expansions along the radial direction produced in particular by vacuum, VV baking, and possible earthquakes. The legs are threaded at the top and they are screwed into stubs in the bottom structure of the VV.

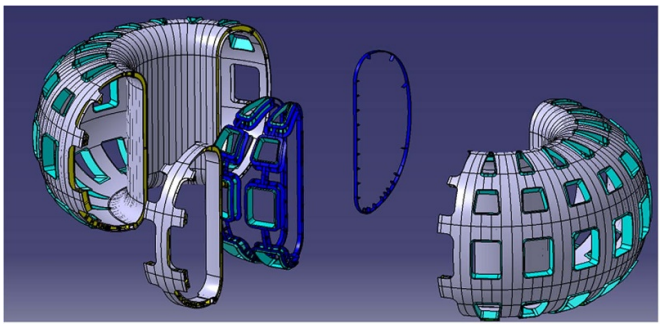

Figure 8. Breakdown of the vacuum vessel sub-components. Reproduced with permission from DTT team.

During normal operation, the double-wall cavity will be filled with water (borated water during high performance plasma operations) as neutron streaming moderator to enhance the neutron shielding capability of the VV, thus limiting the nuclear heating density in the TF WP to acceptable limits. Between the inner and outer shells, perforated poloidal and toroidal ribs provide the necessary rigidity while allowing the water flow in the interspace. The VV material will be austenitic stainless steel with low cobalt content (Co $<$ 0.05 wt%). The typical thickness of VV plates is 10–20 mm for ports, 15 mm for inner/outer shells and stiffening ribs in the double shell structure, 22 mm for the gravity support interface.

For assembly reasons, the VV will be manufactured in two multi-sectors 170° toroidal angle each and one sector of 20°. Port ducts shall be delivered separately, with bellows, and welded after the 360° assembly is complete with the TF and PF coils in place. All interfaces with the in-vessel and out-vessel components have been accurately captured in the tender documents. In order to keep a reasonable flexibility against possible future design changes, supports are constituted by a plate welded on the vessel surface to which the in-vessel components, diagnostics or any other components shall be interfaced with bolted joints.

The VV will be completely covered by a thermal shield (THS) cooled by He flowing at 80 K in order to shield heat coming from the vessel towards the surrounding magnets. The design is in part inspired by that of the KSTAR machine [33] with a single silver coated 3 mm thick stainless steel plate to improve emissivity. On the cold side, a He gas flows at a temperature of 80 K in a suitable system of pipes. The pipes are redundant to ensure operation even in the event of a failure.

Inside the vessel the already described system of 32 in-vessel coils is located. Their layout is described in figure 9. The non-axis-symmetric coils (for the EFC and ELMs mitigation) are coloured in green: they are arranged in three sets of 9 coils each in three layers.

The axis-symmetric coils are in blue; those below the divertor area control the fine sweeping of the strike points, and the ones around the equatorial ports provide the fast vertical control of the plasma position. Finally, the orange structures are passive coils for the plasma stabilization. In order to minimize issues associated to interface management, the same conductor is used in the two types of coils. It, inspired by that of ASDEX

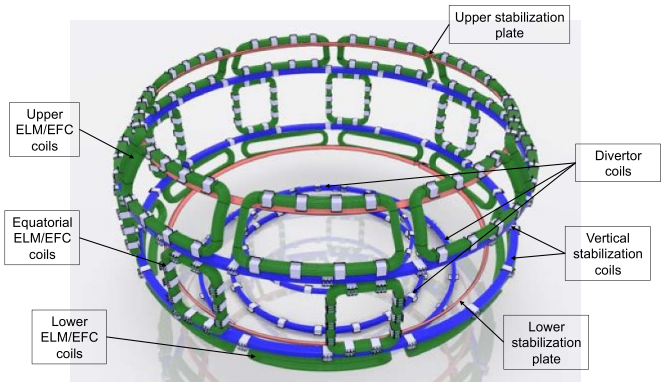

Figure 9. Layout of the in-vessel coils. Reproduced with permission from DTT team.

Figure 10. Render of the cryostat vessel and of the base structure. Reproduced with permission from DTT team.

Upgrade [34], consists of a circular copper conductor with 16 mm external diameter and a central hole, for water flows during dwell time, of 9 mm of diameter. The conductor is inserted in a stainless-steel pipe with 24 mm of external diameter; between the pipe and the conductor an insulating material is foreseen.

The cryostat vessel, with its support base, is also included in the vessel and out-vessel system. The conceptual design, presently on-going, is inspired by that of the JT-60SA machine. The support base is made of 12 columns sustaining 6 beams, radially directed. Columns are located in correspondence of the VV gravity supports, while the 18 TF gravity supports are positioned on a ring located between the two columns. In order to limit the loads on the vessel in case of seismic events, at the top of each column, a seismic bumper is foreseen. At the centre of the base structure, access to the bottom area of the CS is granted for the feeding of the He circuit and of the superconducting coils. A render image of the cryostat vessel is sketched in figure 10.

Finally, also the whole set of auxiliary systems for plasma control belongs to the vessel and out-vessel area. Among them

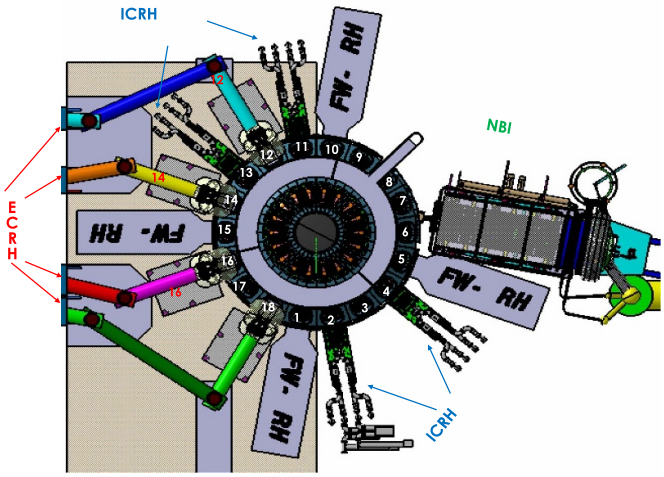

Figure 11. Location of the RH modules. Reproduced with permission from DTT team.

it is worth mentioning, for its role in the exploitation of DTT facility, the divertor pumping system. It consists of a set of 9 cryogenic pumps placed vertically inside 9 ports underneath the divertor. The system shall guarantee 100 m^3 s^{-1} pumping speed and will be operated using He at 4.5 K that is compatible with the requirements of cryoplant. Flexibility in the operation of the divertor pumps is insured by the grouping of the two sets, one with three pumps equally spaced in the toroidal direction by 120°, and another set with 6 pumps spaced by 60°.

3.4. Plasma facing components

In DTT, 54 actively cooled divertor modules are foreseen, 3 for each 20° sector. Out of these, the central modules belonging to the four RH sectors can be used as test modules for the ease of their replacement (figure 11). In view of the first phase of operations, the design of first divertor has been performed jointly with EUROfusion [35]. The poloidal shape has been designed in order to allow a fully compatibility with three families of plasma scenarios (SN, XD, and NT).

Figure 12 shows the poloidal shape of the first DTT divertor with highlighted the position of strike points and baffles. This shape is the result of an intense design activity in which all the constraints associated to the interfaces with cooling system, RH, in-vessel coils and diagnostics have been taken into account. Also, constraints, set-up by the manufacturing process envisaged, have been already included in the design. The W monoblock technology developed for ITER has been chosen in order to reduce R&D activity and insure the construction of the first divertor in time for the first plasma [36–38]. This design has been implemented on the entire plasma facing surface of the divertor in order to allow a large heat load handling capability even of the central horizontal target (dome) and on the outer horizontal target that is necessary to comply with the different magnetic configurations to be investigated by DTT.

Regarding the implications posed by the manufacturing route, it is worth noting the minimum curvature radius equal to

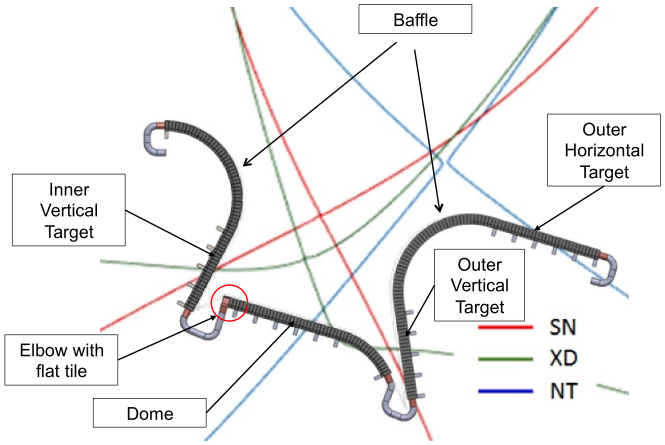

Figure 12. Poloidal shape of first DTT divertor and position of the strike points in the three reference scenarios. Reproduced with permission from DTT team.

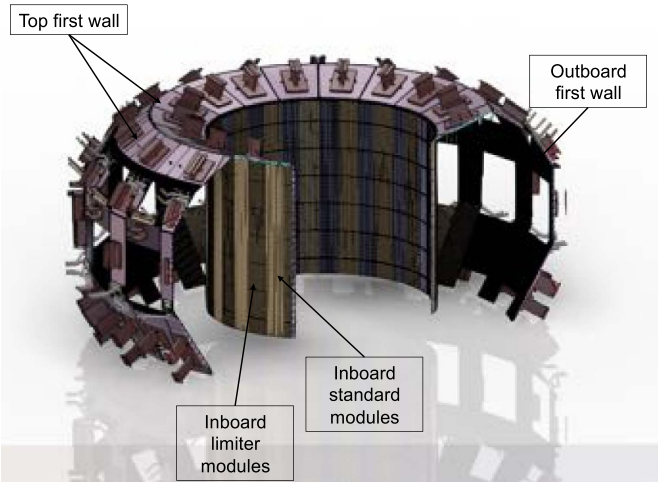

Figure 13. Location of the different first wall components. Reproduced with permission from DTT team.

185 mm is compliant with the thickness of the W monoblock in the pipe direction of 8 mm. Also, the insertion of the swirl tape limits the design to only one curved section for each PFU. Therefore, a specific solution had to be found to shield the 90° bend at the straight side end of the copper tube of the dome PFUs (see figure 12). In order to achieve this, a specific flat tile design has been introduced allowing the manufacturing of the 90° elbow together with the PFU in W monoblocks. The introduction of the flat technology in the PFU for the dome may limit the maximum heat flux in that area and this will be part of the qualification process. Nonetheless, this limitation has been viewed acceptable since it will receive only radiative heating. In any case, a qualification activity is ongoing to assess the flat tile design.

Furthermore, the 90° elbow does not allow the insertion of a swirl tape and this leads to a limit of 17.8 MW m^{-2} for the dome. This is the maximum load allowed to have a margin of 1.4 from the critical heat flux. Tests of PFU mockups are ongoing to qualify the design and to identify the limiting thermal loads and margins. The reduced thickness of the armour (3 mm are compatible with the expected erosion in DTT) allows high stationary loads (greater than those of ITER: 10 MW m^{-2}) also for the dome.

The High Heat Flux tests conducted on the DTT divertor target mock-ups, of 3 and 4 mm armour thickness respectively, highlighted an excellent overall behaviour of the component. The mechanical fatigue resistance of the armour material and of the junction with the cooling tube were verified at the most demanding conditions (high thermal load and high cooling water temperature). The load residence time (10 s) in addition to being suitable for reaching stationary thermo-hydraulic conditions is also effectively comparable with the duration of slow transient events in DTT. The results therefore also correctly take into account deterioration phenomena depending on the residence time at high temperature such as creep and grain growth [39].

Regarding the FW, it is remarkable that it will be water cooled from the beginning of the operations. Four distinct refrigeration circuits are envisaged: one for the limiter modules at the inboard side, one for the standard module at the inboard, one for the top and one for the outboard (figure 13).

To fulfil the stringent operational requirements posed by the plasma configurations and the limitations posed by being RH compatible, four different designs have been considered. In particular, at the inboard the 18 standard modules, made of CuCrZr coaxial pipes coated with W plasma spray to sustain the radiative loads, are interspersed with the limiter modules, made with W monoblocks welded on CuCrZr coaxial pipes. On the outboard two different manufacturing routes are under investigation: one using additive manufacturing, the other using welding. In both cases, the outboard modules (90 in total) are constituted by stainless steel W-coated panels (5 type per sector) with cooling channels inside. Each panel is individually cooled by water feds through the equatorial and the upper lateral ports. The design of the top FW will be similar to that of the inboard limiter modules in order to insure high performances due to disruptions.

Plasma facing components cleaning and conditioning will be done by a combination of baking, glow discharge and boronization [40]. Baking will be performed up to 200 °C (strong baking) heating the VV by replacing the water coolant with hot nitrogen and heating the ports by dedicated electrical heaters installed at the in-vessel surface of the ports for easier replacement in case of failure. Glow discharge cleaning (GDC) in hydrogen and conditioning by boronization will be performed after vessel venting before energizing the TF coils or, if necessary, with the TF switched off at the weekends. Glow discharge will be done with 6 fixed electrodes coplanar with the FW integrated into the lower horizontal ports. Electrodes are actively cooled to remove up to 0.5 MW m^{-2} of expected radiated power during plasma operation. This is to keep their surface at the same temperature as the FW to avoid infrared contamination on IR camera measurements. The active cooling makes more difficult to realize the electrical insulation of the front electrodes plate during the active phase. For this purpose, a ceramic breaker has been proposed to be installed along

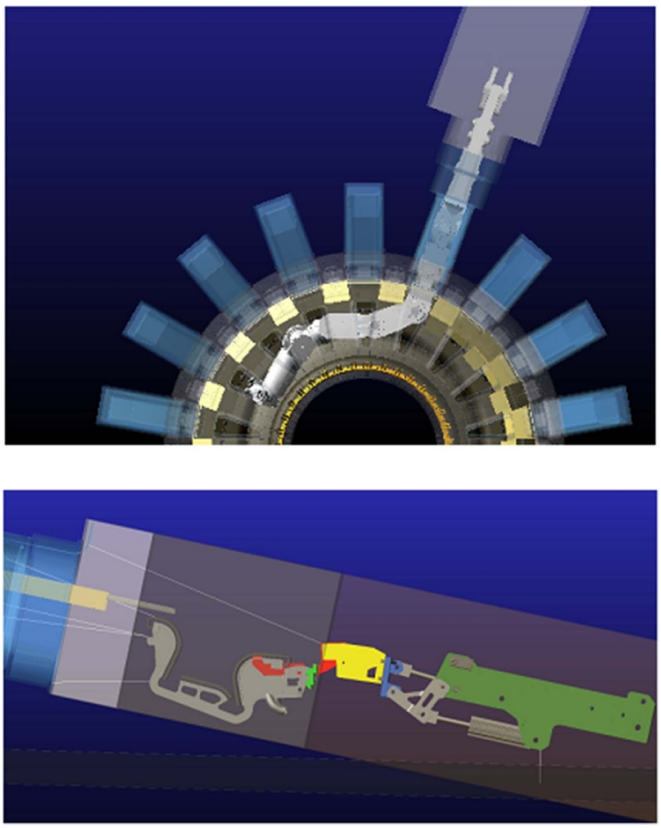

Figure 14. DTT RH equipment: HYRMAN (upper) and CTM-CMM (lower). Reproduced with permission from DTT team.

the cooling pipe run and also a solution similar that one proposed for permanent ITER electrodes is under consideration to avoid water leakage risks. A dedicated gas injection line with 4 toroidal equally distributed locations on the LFS midplane will be used for injecting the He + B_2H_6 mixture during glow discharges for boronization, during this operation the cryopumps will be heated up in order to avoid saturation with boron of the charcoal on the cryopanels.

3.5. RH system

DTT will produce a significant amount of neutrons, with a production rate of up to about $1.5 \cdot 10^{17}$ n s^{-1}, leading to the necessity of a remote maintenance system. Closely related to the in-vessel components design is the specification of the RH system. In DTT, RH will be restricted solely to the in-vessel components due to the relatively low radiation expected in the cryostat. Nonetheless, to limit the duration of the substitution of the divertor system and then to secure the availability of DTT for the experimental campaigns, RH of the in-vessel components is planned to be ready from the beginning of the operation. Two main sub-systems are foreseen: HYRMANs (hyper redundant manipulators) to handle outboard, top and inboard FW modules; and CTM-CMM (cassette toroidal and multifunctional movers) for the removal and installation of the lower divertor (see figure 14).

Requirements posed by the design of RH systems have been shared among all the DTT components. In this respect 4 sectors have been reserved for the RH operations. This will bolster attractiveness of DTT as an experimental facility allowing to test divertor solutions under well defined boundary conditions. In order to prepare the RH operations, expected in the advanced phase of the machine operation, and to upgrade the end-effectors of the base of the updates in the plasma-facing components design, a dedicated training facility is under preparation. It will include a 110° VV sector mock-up.

All the RH sub-systems shall be tested and improved in the facility and, in addition, the training of personnel during the experimental campaign will be carried out to minimize the time needed for RH activities. The scheduled removal of the main divertor is expected to take 6–8 months. The removal and reinstallation of the divertor cassette of a test port is expected to take two weeks. The duration for the repair of a water leak depends on the location of the leak. The cool down plus warm up of the device are expected to take 30 d.

3.6. Diagnostics system

DTT will be equipped with a complete set of machine and plasma diagnostics systems. A two steps approach has been considered so far. First the so-called day 0 diagnostics will be procured and installed for the initial operations, then Full Power Phase diagnostics equipment for advanced plasma control shall be introduced. In line with the main objectives of DTT, particular attention has been devoted to the diagnostics of the pedestal, because of its importance in the determination of the overall confinement and also for the impact that local instabilities, such as Edge Localized Modes, may have on the divertor target. In the divertor region, where the power exhaust is concentrated, the main interest is to unravel the way transport and topology influence the power loss density and particularly the dynamics of the plasma detachment, the condition believed to be essential in DEMO and that requires a delicate and reliable feedback control to be maintained.

The way fuelling techniques, such as pellet or gas puffing, can influence the separatrix density is also of particular interest and a careful knowledge of the neutrals space distribution is deemed to be important. Total and energy resolved radiation (electromagnetic and particle) measurements are fundamental for various tasks such as the evaluation of the power balances, the study of asymmetries in the impurities distribution (poloidal and toroidal), the impact of extrinsic impurities to form a radiation layer and favour the plasma detachment. Particular attention is payed to detection of the ionization in front of the targets, as well as the degree of compression that the divertor can exert on impurities, particularly on helium.

In the definition of the whole set of plasma diagnostics special attention has been devoted to the CAD integration. This is, indeed, a prerequisite in accordance with the strategy of progressive implementation discussed before.

Figure 15 reports a render image of the DTT plasma diagnostics implemented in the CAD model exemplifying the

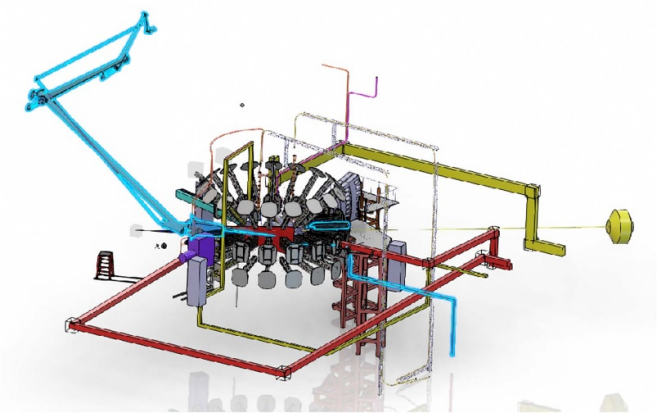

Figure 15. Layout of plasma diagnostics in 3D CAD model showing that each diagnostic system is already fully integrated in the design. Reproduced with permission from DTT team.

traceability of the physical interfaces in the model that introduce constraints in the assembly procedures and the hall layout. The correct tracking of the interfaces made it possible to manage every change that became necessary during the design, with limited impact on the layout.

A table with the list of the day-0 diagnostics is reported in appendix.

3.7. Assembly

The DTT assembly was originally planned according to the initial strategy developed for ITER. This would have had the advantage that the components could have been assembled as soon as they were available. The delay of the availability of the torus hall, where the assembly is also performed, brought to decision to adopt a different strategy based on the KSTAR experience. The machine will be assembled including all the in-vessel components before the start of the integrated commissioning. In order to do that in a limited amount of time, assembly procedures have been carefully studied during the design of each component.

The assembly will be performed mainly in the torus hall where an area will be dedicated to pre-assembly and testing activities and over the cryostat base for the final assembly phase (figure 16). Nonetheless, it is planned to use two of the existing buildings for the pre-assembly of the VV sectors and for CS preassembly. The assembly plan of DTT is constituted by the following main steps:

- Assembly of the cryostat base
- Pre-assembly of the lower PF coils (PF6, PF5, PF4)
- Assembly of the VV multi-sectors cored with the THS
- Insertion of the TF coils and the torus closure through the insertion of the final VV 20° sector
- Final upper PF coils installation followed by the insertion of the CS, fixing He distribution piping and feeders inside the cryostat
- Mounting the in-vessel components (In-vessel coils, FW, divertor, Port Plug, etc)

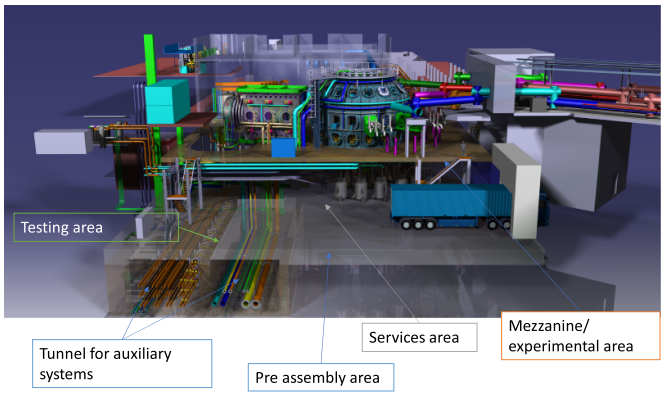

Figure 16. Layout of tokamak in the one of the final phase of the assembly. Reproduced with permission from DTT team.

- Assembling the cryostat THS, the cylindrical body and Top Lid.
- Final Installation of auxiliary systems as FW, DIV, Coils Water coolant System, Feeders, cryogenic system (valve box and cryoline), Vacuum system.

The In-duct diagnostic will be installed with a support structure called ‘Port Plug’, with an approach of Plug and play to allow a fast installation and the removal by RH. Moreover, the port plug will allow to perform the baking (strong and low) of the Diagnostic and Ducts, cooling the diagnostic during the baking phase (if necessary) and during the operation and cooling the end cap of the Port Plug (plasma Facing). The reactor is equipped with 40 ports instrumented with Diagnostic, 4 ICH and 8 ECH that can be installed with the support of the Port Plugs. The Diagnostic that should be installed in the duct at Day 0 involves 18 ports.

Finally, the need of parallel shifts has been identified for a certain amount of in-vessel and ex-vessel mounting operations. The on-site winding activity of the in-vessel coils will be performed by means of a rotating table inside the vessel. The bending machine shall also be mounted internally, while the conductor spool shall be kept on a despooler machine outside. The conductor will be fed inside the vessel through equatorial port in sector 7. To train the operators and set-up the manufacturing procedures, the five axis-symmetric coils (for divertor strike point sweeping and for vertical stabilization of the plasma) will be wound in a pre-assembly area before the torus hall building will be made available. In this area, following the experience of ASDEX Upgrade, a full-scale mock-up of the VV will be constructed. The mock-up will integrate the 30° sector mock-up foreseen in the VV procurement with the remaining 330° simplified in order to provide only the correct interfaces and boundaries. Only after all 32 coils have been assembled; the assembly of the plasma-facing components can start. The FW will be mounted first and then the divertor modules will be inserted through the lower horizontal ports and positioned. In both cases, assembly will be performed with the concurrent participation of four teams each taking care of a 90° section. Figure 16 shows a render image of one of the last phase of the tokamak assembly. One may recognize the

pre-assembly area and the mezzanine for the assembly of the diagnostics.

4. Heating and current drive

4.1. General remarks

DTT will be equipped with three heating systems: ECH, ICH and negative neutral beam injector. A total installed power of 50 MW will be made available progressively in the 3 different stages on which the research plan of DTT is articulated.

Table 3 reports the installed power and the foreseen power coupled to plasma for the three systems. The design guidelines of the heating systems are to rely on consolidated technology and to exploit as much as possible the experience gained by the ITER R&D. On the other hand, the expected lifetime of DTT (25 years) make necessary to exploit novelty that can guarantee support and development for long periods. Finally, DTT will be also the device on which solutions relevant for DEMO can be tested and exploited. Among these are the Solid State Transmitter for ICH, the evacuated multibeam transmission line (MBTL) for ECH and the metal 3D printing for the manufacturing of crucial NBI components.

4.2. ECH system

The DTT ECH system is organized in clusters (see figure 17), each with eight gyrotron sources, one transmission line (TL) and two (equatorial and upper) antennas. This architecture allows easily the modular upgrade foreseen in the DTT operational program: two clusters for the first stage of operation and four clusters for the final stage. In addition of providing the main plasma heating, the ECH system is demanded also to perform many operational tasks such as: assisted breakdown; plasma current ramp-up & ramp down; L–H transition; core heating & current drive; control of MHD modes (as sawtooth and neoclassical tearing modes); profile tailoring; mitigation of impurity accumulation and wall conditioning. The reference microwave source is a diode-type gyrotron, with collector voltage depression, operating at 170 GHz with efficiency >40%, to yield 1 MW for 100 s [41]. A joint procurement with Fusion for Energy was started for the provision of the first 16 gyrotrons for DTT and 6 for ITER. The acceptance of the first DTT gyrotron has taken place at the end of 2023 and the completion of the first cluster within 2028. The RF sources are fed in pairs by a High Voltage Power Supply set, composed of one main PS (−55 kV, 2 × 55 A) and two body PSs (+35 kV, 20 mA), one for each gyrotron. The MBTL concept, to deliver a large number of power lines from the gyrotrons to the tokamak ports, is based on the quasi-optical (QO) propagation of 8 Gaussian beams in a single path, realized by a set of shared focusing and plane mirrors in a confocal arrangement [42]. The mirrors are actively water cooled, through a double-spiral circuit, to minimize surface deformation with heat load in long pulses and maintain the overall losses low enough to provide the goal of 90% of transmission efficiency [43]. One of the novelties included in the design is the enclosure of the TL under vacuum in order to minimize the transmission losses

Table 3. The distribution in time of the HCD power in DTT.

	Phase 1 ($T = 0$)	Phase 2 ($T = 5$y)	Phase 3 ($T = 9$y)
ECH	16 MW/14.4 MW	16 MW/14.4 MW	32 MW/28.8 MW
ICH	4 MW/3 MW	4 MW/3 MW	8 MW/6 MW
NBI	–/–	10 MW/9.5 MW	10 MW/9.5 MW

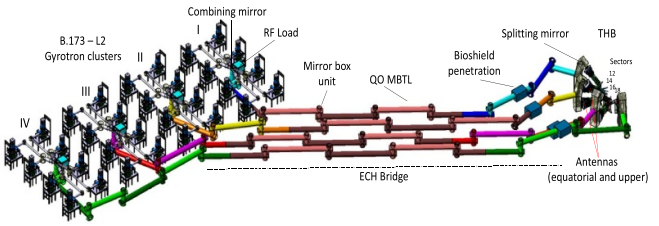

Figure 17. The layout of the whole DTT ECH system. Reproduced with permission from DTT team.

and the arc risks in air. The enclosure contains the mirrors with sustaining structures and follows the whole beams path. Two pumping systems for each TL are foreseen to reach a vacuum level of $\sim 10^{-3}$ Pa. A section of corrugated waveguides (WGs) is inserted between the final section enclosure of the QO lines and the plug-in antenna in order to reduce the vacuum conductance, avoiding effect on plasma operation. In fact, only a gate valve along this WG separates the MBTL vacuum from the one of the tokamak vessel, normally closed and opened only during the ECRH pulse. A back-up option with the later insertion of a diamond window before the valve, in case of unexpected difficulties during plasma operations, has been considered in the design. The model of mirrors lines has been analysed with electromagnetic simulations to evaluate the losses due to the geometry and finite (mirrors) dimension effects. Up to ∼1.5% of losses due to spill-over have been found after the reflections on 29 mirrors of the longest MBTL, while an average 3% of losses are due to the converted modes not coupled into the WG. Ideal ohmic losses in the range ∼4.5% (evaluated for first two clusters) have to be added to estimate an overall efficiency of 90.6%, including the transmission losses (0.5%) at the QO-WG-QO transition at launcher entrance. Analysis of thermal deformation effects and misalignments occurring along the line will complete the characterization, defining the system requirements for the engineering design phase.

The concept of the antennas (based on the front-steering concept) is designed on very compact modules, each with identical features and independent to each other, to increase the flexibility of the system [44, 45]. The single launcher module is composed of two mirrors: a fixed shaped mirror (M1) to refocus the microwave beam coming from the WG section and a steerable plane mirror (M2) to direct the beam in the desired location (see figure 18(*a*)). For the equatorial antenna the launching mirrors are capable of covering a steering range of 35° in the poloidal direction and 50° in the toroidal direction, while for the upper antenna the ranges are 55° and 45° respectively. Several R&D activities are undergoing as the selection of the actuator for M2, the design of driving mechanism and the identification of the position sensors. A

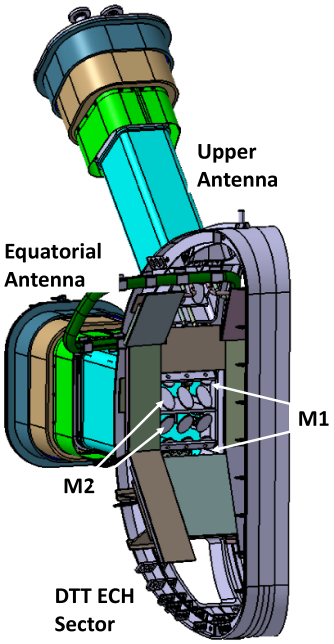

(a)

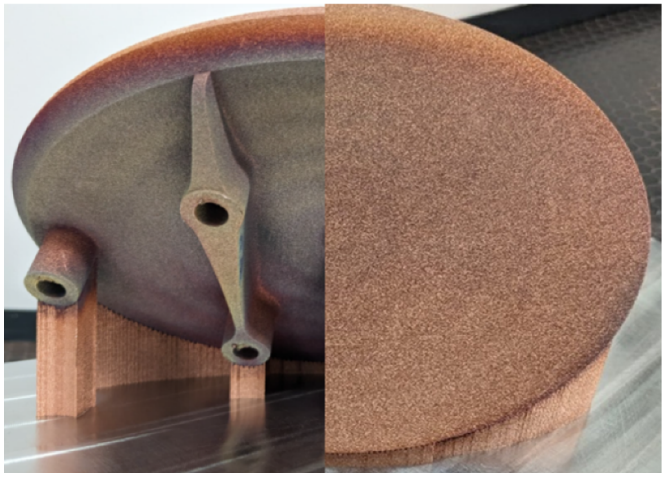

(b)

Figure 18. Side view of upper and equatorial antenna of one ECH cluster (*a*); launcher mirror (M1) raw blank from additive manufacturing (front and rear views) (*b*). Reproduced with permission from DTT team.

novelty could be the use of an in-vessel actuator for M2: it is compact to fit the limited space available inside the ports, does not require mechanical vacuum feedthroughs, it is lightweight, fast (1°/50 ms) and has an accuracy in the positioning better than 0.1°. The present candidate is a piezoelectric walking drives [46], with the main drawback of low driving force in an environment where magnetic torques can be very high.

Torques are due to the interaction of the static magnetic field with the currents induced in the mirrors by variable magnetic fields, as the non-axisymmetric in-vessel coils for plasma

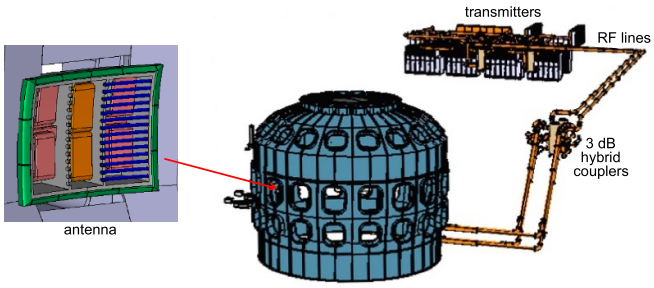

Figure 19. Layout of the ICH system of DTT and antenna front (part of the Faraday screen was omitted to make the interior visible). Reproduced with permission from DTT team.

control, and especially in case of plasma current quench during disruption events [47]. To minimize the resistive forces acting on the system, different solutions have been also investigated for the launcher mirrors, as different materials and cooling strategies to reduce weight and eddy currents during operation. First prototype of M1 in CuCrZr alloy has been realized by Additive Manufacturing [48], at the DIAM lab, Padova section of INFN (see figure 18(*b*)). The next goal is to perform high-power tests by using the first DTT gyrotron to validate this manufacturing technique, capable to realize challenging cooling channels and to reduce costs.

4.3. ICH system

The ICH system of DTT is organized in modules, each made of four transmitters and two antennas. A panoramic view of the first module is depicted in figure 19. The system is aimed at providing RF power in the frequency range between 60 and 90 MHz [49] to be delivered for:

- DTT experiments: around 1.5 MW per antenna for the ion heating in the reference scenario, mostly via ^{3}He or H minority heating. A contribution to applications beyond heating, especially the generation of fast particles, is expected too.
- Wall conditioning: less than 100 kW per antenna for wall cleaning and deposition of materials with low atomic number over DTT FW (i.e. boronization).

In DTT a plug antenna, thus with size smaller than port cross-section, would have to operate at power densities never achieved so far with H-mode ELMy plasmas, as reported in a survey described in [50]. Having a high reliability as requirement for ICH power coupling, an antenna solutions larger than the port duct has been conceived, requiring remote-handling system to be installed and then maintained because of DTT activation after high performance operations. A three-strap antenna concept was identified as the best trade-off between available space, maximization of coupled power, and availability of some control on parallel electric near fields and on low parallel wavevector spectral components. The antenna, whose geometry is sketched in figure 19, is in the pre-engineering design phase [50]. Preliminary calculations demonstrate that a

power larger than 1.5 MW can be coupled over most of the frequency range with a radially movable cantilevered launcher, operating at 30 mm from the separatrix. The poloidal curvature of the antenna does not follow the separatrix profile in the reference scenario, but it is slightly relaxed to allow the launcher to park behind the FW when not in use. Several critical aspects are under assessment as for example antenna materials and cooling.

As far as plasma facing components are concerned, uncooled Faraday screen bars do not exceed the recrystallization temperature only if made of TZM. As to antenna side limiters, a heat load of 2.5 MW m^{-2} was estimated, pushing for the use of ITER divertor technology, i.e. Tungsten monoblocks, but more accurate 3D evaluations of the particle flux are ongoing. The interface with the RH system and the development of quick RF connectors for the antenna feeds are the major points of concerns because they require a significant development. A modification of the RHS dexterous arm is under consideration to operate with the heavy antenna frontend.

The design of RF feedthroughs focused on two competing solutions that consist in alumina windows either with a conical shape or based on a disk with non-uniform thickness. Preliminary thermo-mechanical analyses suggest that active cooling is not necessary if the feedthrough is outside the port plug, i.e. it can rely on natural convection, and its main structures, made of titanium and stainless steel, are coated with copper or silver.

RF lines will rely on standard uncooled 9 3/16″ rigid coaxial cables with characteristic impedance of 50 Ohm over most of the line and 30 Ohm close to the antenna. The precise position for the variation of characteristic impedance is being studied. Classical impedance transformers are envisaged with an external ELM-resilient matching scheme based on 3 dB hybrid couplers [51]. Hybrid coupler outputs are connected to the straps of different antennas.

Unlike ITER transmitters that still rely on tetrode-based cavity amplifiers, those for DTT will be completely based on solid-state technology. To the best of authors' knowledge, they will be the first ones of this kind, i.e. with such an unprecedented combination of power, frequency range and pulse duration for such technology. Such choice is the result of a deep internal discussion and a market survey that highlighted its numerous advantages such as reliability, lifetime, modularity, redundancy, absence of high voltage and x-ray shielding, easy maintenance, large-scale production of the active components, and reproducibility of equivalent spare parts. Taking into account technology maturity, documented efficiency of ICH systems, and some design margin, a conservative output power of 1.2 MW per transmitter was defined with a slew rate of the order of 0.5 ms and shutoff time of a few μs.

4.4. The NBI system

The negative ion based NBI represents one of the most complex and challenging subsystems of the DTT project. It is meant to inject into the plasma deuterium neutrals (D^0) with an energy of 510 keV and a total power of 10 MW. The beam enters the plasma tangentially in the same direction of the plasma current, with an average tangency radius $\sim$ 1.95 m, corresponding to an injection angle of 35° at the radius of 3.4 m. In order to enlarge the NBI operational window to lower plasma densities, the system is being designed to allow beam energy and power modulation, thanks to electrostatic grid optical optimization. In the considered plasma scenarios, shine-through losses become significant only below $1 \cdot 10^{20}$ m^{-3}, which is half the reference line-averaged plasma density [52].

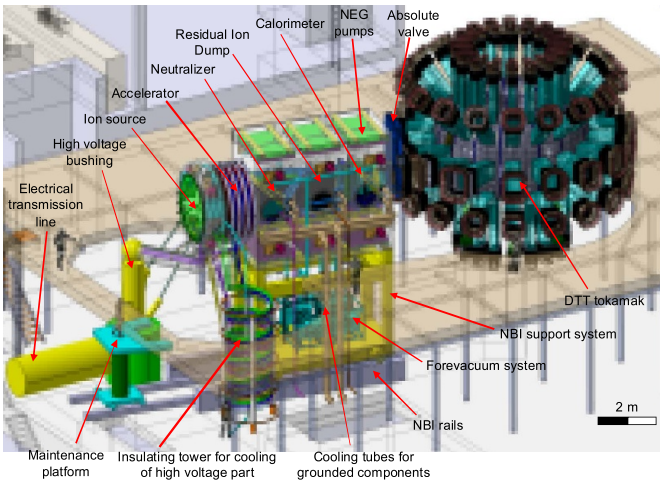

Figure 20. Overview of the conceptual design of the beamline for the DTT NBI (2023 status). Reproduced with permission from DTT team.

An overview of the current conceptual design of the beamline for the DTT NBI is given in figure 20.

The design adopted for DTT NBI, i.e. the assembly of the accelerator and ion source connected to the back part of the **VV** is similar to those of JT-60 [53] and LHD [54] with an air-insulated beam source. This solution was selected to maximize reliability and availability by simplifying the design and improving beam source accessibility. The differences in the DTT NBI design from the previous schemes is in the type of ion source: in fact, the same concept adopted for ITER, based on Radio Frequency source, mainly developed by IPP Garching [55], is proposed to be used. The beam line components, composed of the Neutralizer, the Calorimeter and the residual ion dump, will be ITER-like too, whereas any large flanges will not be included in the VV in order to reduce cost and weight.

The DTT NBI is required to operate with high efficiency in several operating scenarios, i.e. in a large range of beam energies, between 10% and 100% of the nominal value (510 keV). To reach this challenging goal, an innovative accelerator concept has been developed, based on the Spherical and Lemon Hyperlens Grid concept [56]. The implementation of this design concept of the accelerator is possible only thanks to recent improvements of the additive manufacturing technology, which permits to build more complex geometries that were not feasible using traditional techniques [57].

The electrostatic acceleration is to be implemented with grids of increasing potentials from −500 kV to 0 kV. A dedicated power supply, the acceleration grid power supply (AGPS) made of three stages of 167 kV each in series, is foreseen to provide the required voltages and currents (60 A). Since the grids are spaced at the limit of the voltage holding in vacuum, breakdowns between the grids are expected to occur frequently. The AGPS must withstand these events, by interrupting the delivery of the power to the load as quickly as possible, to limit the energy transferred to the arc, which could damage the grids. Two possible schemes for the AGPS are under evaluation. In addition to a solution based on ITER/MITICA AGPS, an alternative option is being considered. It would deploy the modular multilevel converter (MMC) technology, which is used in HVDC transmission, but would be a novelty in the field of HV power supply for NBIs [58, 59]. However, since the submodules of the MMC are air-insulated, the volume occupied by the converter would not be compatible with the existing buildings assigned to the AGPS. A possible solution would consist of installing the AGPS in a free area far from the tokamak and connected to the load with HV coaxial cables, about 700 m long. This alternative is at present under careful evaluation [60].

A third relevant innovation of the DTT NBI, compared to the existing devices, regards the vacuum pumping system, which will be based on non-evaporable getter (NEG) pumps [61]. This will represent the first application of the NEG technology to an NBI for the heating and current drive system of a fusion experiment, with a possible simplification of the overall construction compared to typical solutions with cryogenic pumps. The design has been optimized in terms of the most relevant aspects, i.e. the pumping capability, the margin against danger of deuterium ignition and the margin against embrittlement of the getter material. Based on the preliminary study carried out so far, it appears that the usage of the NEG pumps in DTT NBI could be possible, as all the DTT NBI requirements could be achieved with this system. More detailed studies on the optimization of cartridge number and layout, thermal aspects, maintenance strategy, electrical connections and mechanical supports will be carried out in the next future.

Various design options have been considered for the whole system and a comprehensive set of simulations has been carried out, using several physics and engineering codes to guide the choice of the most suitable design options and to optimize them, with the aim of finding a good compromise among different design requirements. These simulations regard mainly the efficiency of the main processes, the optics of the beam, the physics reactions along the beamline (stripping, charge-exchange and ionization), the thermo-mechanical behaviour of the acceleration grids and the coupling between the beam and the plasma in the tokamak chamber. Based on the current design, the wall-plug efficiency of the whole NBI system is foreseen to be around 35%. This is the product of the main efficiency of the system, i.e. auxiliaries/extraction efficiency (90%), accelerator efficiency (80%), beam source/neutraliser entrance transmission efficiency (95%), neutralizer efficiency (55%) and beam line/duct transmission efficiency (95%).

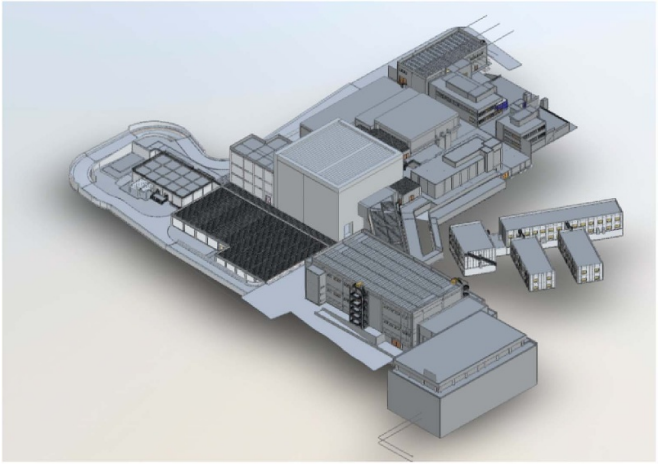

Figure 21. DTT project buildings. Reproduced with permission from DTT team.

5. Balance of plant

The Balance of Plant includes all plant infrastructural/supporting facilities and auxiliary/utilities systems needed to keep the plant running stably and efficiently. This includes the cooling system, the buildings and site modifications, the electrical distribution system, the Control/Safety, the Telecommunication and Security Systems.

DTT is a 'brown field' project that will involve existing building and facilities.

The new buildings amount to about 150.000 m^3 and the existing buildings to be adapted for the DTT systems amount to about 12.000 m^2 (figure 21). The definitive design has been completed and will be followed by the verification by a third party. The call for tender will be launched in 2024. A number of preparatory activities are ongoing to facilitate the execution of the new building construction and de-risk the project schedule. Specifically, two contracts for the opening of the new construction site gates and the demolition of two buildings will be placed for this purpose.

The electrical network system has to provide 'steady' loads with an absorbed power of 40 MVA and 'pulsed' loads with an absorbed power of about 250 MVA. As shown in figure 22 a High Voltage line is foreseen from the point of connection of the National Grid at 150 kV to the new 150/20 kV main substation (SS0) followed by a medium/low voltage line to 5 distribution substations (SS1–SS2–SS3–SS4–SS5). There is also an emergency power generation system composed of a few emergency diesel generators, which supplies part of the low voltage loads in case the main supply is unavailable, and the uninterruptible power systems to supply the safety and vital loads.

The DTT cooling system has been designed on the basis of the assumption of a flat top at maximum parameters up to 50 s and maximum dwell time for high performance of 3600 s.

The VV temperature during normal operation is up to 60 °C. Baking can be carried out either at 110 °C using water and 200 °C using nitrogen.

Figure 22. DTT electrical network system. Reproduced with permission from DTT team.

6. Preparation of the research plan

The DTT design and construction activities are accompanied by intensive physics studies, carried out by various Italian institutes with international collaborations, including theory, scenario modelling, diagnostics and control schemes developments. Building on these studies, the first version of the DTT research plan (DTT-RP) has been prepared by a European team, involving more than 90 participants from various EUROfusion partners, and will be publicly issued soon. It should be stressed that the DTT-RP is a living document, which will be regularly updated during the construction phase and which will constitute the basis for the construction of the DTT scientific programme and of subsequent device upgrades. It will also catalyse and guide the research activities in preparation of the experimental phase. In the elaboration of the DTT-RP, ITER and EU-DEMO groups have been informed and consulted. In the future, the participation of international partners will be very welcome and is expected to enrich the scientific vision and programme of the DTT project.

The DTT-RP document describes the objectives and research strategy of the DTT experiment, culminating in a set of programmatic headlines, organised following the main research phases of the device, characterised by the progressive upgrades of the heating power and other sub-systems. The main top-level headlines of the DTT scientific contribution to the European fusion programme, in support to ITER and in preparation of DEMO are the following:

- Development and assessment of baseline and advanced scenarios for the various divertor configurations available, at nominal field and current, for performance comparison.
- Development of scenarios at half field and current, with 2nd harmonic ECRH heating, to study high β_N regimes. These studies, carried out in a full tungsten device, will complement those performed by JT-60SA with carbon PFC.
- Extensive disruption and runaway electrons studies, including mitigation by SPI, in support of ITER.
- Detached regimes optimization and control by impurity seeding in various scenarios.
- Evaluation of λ_q at high TF; comparison with theory and scalings.
- Development of small/no ELMs scenarios and their control with non-axisymmetric coils and pellets.
- Wall erosion, W migration, D retention and removal studies and assessment in view of application to DEMO.
- Extensive testing with the Divertor Test Modules for new FW and divertor materials.
- Transport, MHD, EP physics studies with reactor relevant dimensionless parameters.

Details of the Research Plan can be found in [12].

7. Conclusions

DTT is in the construction phase with about one third of the construction budget already committed in industrial contracts. All the permissions for the construction have been granted together with the licensing for cat. A ionizing radiation source. The design of the new buildings has been completed and that of the electrical distribution system (including the new 150 kV/20 kV switchyard) is being completed and in 2024 the call for tender for both will be launched. The construction of the 150 kV line has been approved and is in progress. The characteristics of the first divertor have been agreed with EUROfusion and the engineering activity is progressing. The preparation of the Research Plan has started in collaboration with all the EUROfusion laboratories.

Acknowledgments

This work has been partially carried out within the framework of the EUROfusion Consortium, funded by the European Union via the Euratom Research and Training Programme (Grant Agreement No. 101052200—EUROfusion). Views and opinions expressed are however those of the author(s) only and do not necessarily reflect those of the European Union or the European Commission.

Among all the authors, a special mention goes to G. Granucci, R. Martone, P. Martin, A. Pizzuto and G. M. Polli for the valuable contribution provided in the collection of contributions, in the definition of the layout of the paper and in the compilation of the text.

Appendix. Day 0 diagnostic systems

Diagnostic systems	Measured parameter
Tomography and SXR imaging	
Bolometers cameras core and divertor (160 channels/200 total)	Radiation Total, profile
SXR Sensors (70 channels/100 total)	SXR profile
SXR Imaging	Fluctuations, MHD—SXR profile
Interferometry and polarimetry	
Interferometer Vertical (Central LOS) (4–5 cords)	Fluctuations, electron density
Interferometer Tangential	Fluctuations, electron density
Active and passive spectroscopy	
Charge Exchange and Diagnostic Neutral Beam ChargeExchange (CXRS)	Ion temperature, Profile: core/pedestal/SOL Rotation, toroidal—poloidal
Diagnostic Neutral Beam Injection (DNBI) and MSE Polarimeter	Safety factor, Current profile
SXR Crystal spectrometer	Impurities, density profile
SXR spectrometer (XUV1) and (XUV2)	Impurities, species monitoring
Visible D alpha array and Divertor	Neutrals Density and Fluctuations ELMs and L-H transition, Recycling
Visible spectrometer survey and Divertor	Wall, chemical composition monitor, isotope ratio/Impurities, radiation power of each species and ionition front (Divertor)
Visible Z_{eff} Bremsstrahlung	Impurities, Z_{eff} profile
VUV Spectrometer Edge	Wall, density and detachment and enrichment
VUV Spectrometer Survey	Impurities, species monitoring
Diagnostic systems	Measured parameter
Neutrons and gammas	
Neutrons Activation Foils	Neutrons, Yield
Neutrons Yield Monitors	Neutrons, flux monitor
Magnetic sensors	
Biaxial LTCC Coils IN-VESSEL	Plasma shape & equilib. Reconstruction—Vertical speed estimation—MHD fluctuation
Biaxial Pick-up Coils EX-VESSEL and IN-VESSEL and DIVERTOR	Plasma curr. & centroid posit. Estim.—Plasma shape & equilib. Reconstruction—Vertical speed estimation
Current Shunt IN-VESSEL and DIVERTOR	Halo and Eddy currents
Diamagnetic Loops Compensation Coils EX-VESSEL and IN-VESSEL	Plasma magnetic energy estimation
Diamagnetic Loops EX-VESSEL and IN-VESSEL	Plasma magnetic energy estimation
Flux Loops EX-VESSEL and IN-VESSEL	Plasma shape & equilib. Reconstruction—Loop voltage estimation—Eddy current estimation
Hall Probes EX-VESSEL	Plasma shape & equilib. Reconstruction—Magnetic calibration
Optic Fibre Plasma Current—EX-VESSEL	Optic fibre plasma current measurement
Partial Rogoski Coils IN-VESSEL and DIVERTOR	Halo and Eddy currents
Rogoski Coils EX-VESSEL	Plasma Current
Saddle Loops EX-VESSEL	Backup for: Plasma shape & equilibrium reconstruction—Error field reconstruction
Embedded, IR/VIS cameras and PWI diagnostics	
Cameras IR SLOW	Electron temperature, First Wall and Divertor

(Continued.)

(Continued.)

Diagnostic systems	Measured parameter
Cameras IR FAST	Electron temperature, First Wall and Divertor
Cameras VIS	Wall, sources and main gas/Offline inspection
Langmuir probes FW EXTERNAL—INNER	Electron density & electron temperature, density (low power) profile/leg position
Langmuir probes DIVERTOR	Density electron & Temperature electron, density (low power) profile/leg position
Long Term Samples (LTS)	Wall, Plasma Wall Interaction
Microbalance probes redeposition	Wall, ri-deposition layers
Neutrals Gas Analyzer	Neutral Gas Composition
Optical sensors of deformation-strain sensors (FOS) DIVERTOR	Strain and stress deformation
Penning spectroscopy	Gas pressure and composition (Divertor)
Thermocouples DIVERTOR	Wall, temperature
Thermocouples FW EXTERNAL and INNER	Wall, temperature
ECE diagnostics	
ECE Electron Cyclotron Emission Radiometer and Michelson Interferometer	Temperature electron, Profile and Temperature electron, Profile (fast)
Reflectometry	
IN-VESSEL Reflectometry Density Profile Reconstruction (DPR)	Density profile
Thomson scattering systems	
Thomson Scattering Core-Edge (Inner) LIDAR	Density electron Profile/Temperature electron Profile (core/pedestal/SOL)
Diagnostic systems	Measured parameter
Run aways diagnostics	
Runaway Electron Imaging Spectrometer (REIS)	RunAways electrons spectrum
Fast particles diagnostics	
Hard-X-rays/Gammas Rays Monitors	Hard-X and Run-Away Monitor

ORCID iD

Francesco Romanelli https://orcid.org/0000-0001-9778-1090

References

[1] Romanelli F. *et al* 2012 *Fusion Electricity: A Roadmap to the Realisation of Fusion Energy* (European Fusion Development Agreement EFDA)
[2] EUROfusion Programme Management Unit 2018 *European Research Roadmap to the Realisation of Fusion Energy* (EUROfusion Programme Management Unit)
[3] Martone R. *et al* (ed) 2019 *Divertor Tokamak Test Facility Interim Design Report 2019* (ENEA) (available at: www.dtt-project.it/DTT_IDR_2019_WEB.pdf)
[4] Pizzuto A. *et al* (ed) 2015 *Divertor Tokamak Test Facility Project Proposal* (ENEA) (available at: www.dtt-project.it/images/DTT_Books/DTT_ProjectProposal_July2015.pdf)
[5] Giorgetti F., Lombroni R., Belardi V.G., Calabrò G., Dalla Palma M., Fanelli P., Fulici M., Ramogida G. and Vivio F. 2022 *Fusion Eng. Des.* **184** 113273
[6] Romanelli M. *et al* 2014 *Plasma Fusion Res.* **9** 34030231–4
[7] Fable E., Angioni C., Ivanov A.A., Lackner K., Maj O., Yu S., Medvedev, Pautasso G. and Pereverzev G.V. 2013 *Nucl. Fusion* **53** 033002
[8] Staebler G.M., Candy J., Belli E.A., Kinsey J.E., Bonanomi N. and Patel B. 2021 *Plasma Phys. Control. Fusion* **63** 015013
[9] Bourdelle C. *et al* 2016 *Plasma Phys. Control. Fusion* **58** 014036
[10] Casiraghi I. *et al* 2023 *Plasma Phys. Control. Fusion* **65** 035017
[11] Innocente P., Ambrosino R., Brezinsek S., Calabrò G., Castaldo A., Crisanti F., Dose G., Neu R. and Roccella S. 2022 *Nucl. Mater. Energy* **33** 101276
[12] Crisanti F. *et al* 2024 *Nucl. Fusion* **64** 106040
[13] Fajardo D., Angioni C., Maget P. and Manas P. 2022 *Plasma Phys. Control. Fusion* **64** 055017
[14] Houlberg W.A., Shaing K.C., Hirshman S.P. and Zarnstorff M.C. 1997 *Phys. Plasmas* **4** 3230–42
[15] Baiocchi B. *et al* 2023 *Nucl. Fusion* **63** 106009
[16] Bonanomi N. *et al* 2023 Full-radius time-dependent simulations of the DTT tokamak plasmas *49th EPS Conf. on Plasma Physics* (*Bordeaux*, *July 2023*)
[17] Fusco V. *et al* 2022 Stability analysis of low-n modes for the Divertor Tokamak Test facility *48th EPS Conf. on Plasma Physics* (*Virtual conference*, *June 2022*) vol 46A (available at: https://info.fusion.ciemat.es/OCS/EPS2022PAP/pdf/P2a.125.pdf)

[18] Porcelli F., Boucher D. and Rosenbluth M.N. 1996 *Plasma Phys. Control. Fusion* **38** 2163–86
[19] Kadomtsev B.B. 1976 *Sov. J. Plasma Phys.* **2** 389
[20] Spizzo G. *et al* 2021 *Nucl. Fusion* **61** 116016
[21] Vincenzi P. *et al* 2023 *Fusion Eng. Des.* **189** 113436
[22] Vlad G. *et al* 2021 *Nucl. Fusion* **61** 116026
[23] Balbinot L., Rubino G. and Innocente P. 2021 *Nucl. Mater. Energy* **27** 100952
[24] Eich T. *et al* 2013 *Nucl. Fusion* **53** 093031
[25] Di Zenobio A. *et al* 2022 *IEEE Trans. Appl. Supercond.* **32** 4201005
[26] Bonifetto R., De Bastiani M., Zenobio A.D., Muzzi L., Turtu S., Zanino R. and Zappatore A. 2022 *IEEE Trans. Appl. Supercond.* **32** 4204007
[27] Romanelli G. *et al* 2023 *Fusion Eng. Des.* **192** 113588
[28] Giannini L. *et al* 2021 *IEEE Trans. Appl. Supercond.* **31** 4201505
[29] Giannini L., Muzzi L., Di Zenobio A., Romanelli G., Zoboli L., Turtù S. and della Corte A. 2022 *IEEE Trans. Appl. Supercond.* **32** 4203205
[30] Lampasi A. *et al* 2023 *Fusion Eng. Des.* **188** 113442
[31] Lampasi A. *et al* 2023 *Fusion Eng. Des.* **187** 113366
[32] Griva G., Musumeci S., Bojoi R., Zito P., Bifaretti S. and Lampasi A. 2023 *Fusion Eng. Des.* **189** 113473
[33] Kim G.H. *et al* 2009 *Fusion Eng. Des.* **84** 1043–8
[34] Herrmann A. *et al* 2019 *Fusion Eng. Des.* **146 Part A** 920–3
[35] Roccella S. *et al* 2024 *IEEE Trans. Plasma Sci.* 1–4
[36] Gavila P., Riccardi B., Pintsuk G., Ritz G., Kuznetsov V. and Durocher A. 2015 *Fusion Eng. Des.* **98–99** 1305–9
[37] Hirai T. *et al* 2015 *J. Nucl. Mater.* **463** 48758
[38] Grosman A., Bucalossi J., Doceul L., Escourbiac F., Lipa M., Merola M., Missirlian M., Pitts R.A., Samaille F. and Tsitrone E. 2013 *Fusion Eng. Des.* **88** 497–500
[39] Roccella S. *et al* 2024 *IEEE Trans. Plasma Sci.* 1–7
[40] Rubino G. *et al* 2024 *IEEE Trans. Plasma Sci.* 1–7
[41] Garavaglia S. *et al* 2021 *Fusion Eng. Des.* **168** 112678
[42] Bruschi A. *et al* 2022 *Fusion Eng. Des.* **194** 113727
[43] Salvitti A. *et al* 2024 *Fusion Eng. Des.* **201** 114228
[44] Fanale F. *et al* 2023 *Fusion Eng. Des.* **192** 113797
[45] Allio A. *et al* 2022 *IEEE Trans. Plasma Sci.* **50** 4054–9
[46] Busi D., Braghin F., Bruschi A., Garavaglia S., Granucci G. and Romano A. 2022 *Fusion Eng. Des.* **180** 113196
[47] Busi D. 2023 *Fusion Eng. Des.* **191** 113550
[48] Bonesso M., Rebesan P., Gennari C., Mancin S., Dima R., Pepato A. and Calliari I. 2021 *Berg Huettenmaenn Monatsh* **166** 256–62
[49] Cardinali A., Baiocchi B., Castaldo C., Bilato R., Brambilla M., Casiraghi I., Ceccuzzi S., Napoli F., Ravera G.L. and Tuccillo A.A. 2022 *J. Phys.: Conf. Ser.* **2397** 012017
[50] Ceccuzzi S. *et al* 2023 *AIP Conf. Proc.* **2984** 030015
[51] Ravera G.L. *et al* 2021 *Fusion Eng. Des.* **166** 12280
[52] Vincenzi P. *et al* 2023 *Fusion Eng. Des.* **189** 113436
[53] Kojima A. *et al* 2015 *Nucl. Fusion* **55** 063006
[54] Takeiri Y. *et al* 2006 *Nucl. Fusion* **46** S199–210
[55] Heinemann B., Fantz U., Kraus W., Wünderlich D., Bonomo F., Froeschle M., Mario I., Nocentini R., Riedl R. and Wimmer C. 2018 *Fusion Eng. Des.* **136** 569–74
[56] Veronese F., Agostinetti P., Murari A. and Pepato A. 2022 *IEEE Trans. Plasma Sci.* **50** 4033–8
[57] Favero G. *et al* 2022 *Int. J. Heat Mass Transfer* **135** 106128
[58] Ferro A., Lucchini F., Agostinetti P., Ratti D., Granucci G., Romano A., Romano R., Cucchiaro A. and Princiotta A. 2021 *Fusion Eng. Des.* **169** 112624
[59] Santoro F., Ferro A., De Nardi M. and Gaio E. 2022 *IEEE Trans. Plasma Sci.* **50** 403350
[60] Santoro F., Ferro A., Murari A., Granucci G. and Romano R. 2023 *Fusion Eng. Des.* **187** 113356
[61] Agostinetti P. *et al* 2023 *Fusion Eng. Des.* **192** 113638